

**Key Points:**

- Austroalpine nappes in the Gurktal Alps east of the Tauern Window experienced alternating phases of enhanced and slow exhumation
- Nappes at higher structural levels were exhumed during Late-Cretaceous extension and have been at upper-crustal levels since then
- The Radenthein and Millstatt Complexes experienced enhanced exhumation during the Middle Eocene and since the Early Miocene

**Supporting Information:**

Supporting Information may be found in the online version of this article.

**Correspondence to:**

A. Wölfler,  
woelfler@geowi.uni-hannover.de

**Citation:**

Wölfler, A., Wolff, R., Hampel, A., Hetzel, R., & Dunkl, I. (2023). Phases of enhanced exhumation during the Cretaceous and Cenozoic orogenies in the Eastern European Alps: New insights from thermochronological data and thermokinematic modeling. *Tectonics*, 42, e2022TC007698. <https://doi.org/10.1029/2022TC007698>

Received 28 NOV 2022

Accepted 7 AUG 2023

**Author Contributions:**

- Conceptualization:** Andreas Wölfler, Andrea Hampel, Ralf Hetzel  
**Data curation:** Andreas Wölfler  
**Formal analysis:** Andreas Wölfler  
**Investigation:** Andreas Wölfler, Reinhard Wolff, Andrea Hampel, Ralf Hetzel, István Dunkl  
**Methodology:** Andreas Wölfler, Reinhard Wolff, István Dunkl  
**Project Administration:** Andrea Hampel  
**Software:** Reinhard Wolff  
**Supervision:** Andrea Hampel, Ralf Hetzel

© Wiley Periodicals LLC. The Authors. This is an open access article under the terms of the Creative Commons Attribution License, which permits use, distribution and reproduction in any medium, provided the original work is properly cited.

## Phases of Enhanced Exhumation During the Cretaceous and Cenozoic Orogenies in the Eastern European Alps: New Insights From Thermochronological Data and Thermokinematic Modeling

Andreas Wölfler<sup>1</sup> , Reinhard Wolff<sup>2</sup> , Andrea Hampel<sup>1</sup> , Ralf Hetzel<sup>2</sup> , and István Dunkl<sup>3</sup> 

<sup>1</sup>Institut für Geologie, Leibniz Universität Hannover, Hannover, Germany, <sup>2</sup>Institut für Geologie und Paläontologie, Universität Münster, Münster, Germany, <sup>3</sup>Geowissenschaftliches Zentrum der Universität Göttingen, Abteilung Sedimentologie/Umweltgeologie, Göttingen, Germany

**Abstract** Austroalpine nappes in the Eastern European Alps have preserved the record of orogenies in the Cretaceous and Cenozoic but their cooling and exhumation history remains poorly constrained. Here we use low-temperature thermochronology and thermokinematic modeling to unravel the exhumation history of the Austroalpine nappes in the Gurktal Alps. Our data reveal marked differences between the exhumation of units located at different positions within the nappe stack and relative to the Adriatic indenter. Units located at a high structural level and farther away from the indenter cooled through the zircon fission track closure temperature in the Late Cretaceous and have resided at depths of  $\leq 5$ –6 km since the Oligocene, as indicated by apatite fission track ages of 35–30 Ma. Thermokinematic modeling constrained that these units experienced enhanced exhumation ( $\sim 0.60$  km/Ma) between  $\sim 99$  and  $\sim 83$  Ma due to syn- to late-orogenic Late Cretaceous extension. After a phase of slow exhumation ( $\sim 0.02$  km/Ma), the exhumation rate increased to  $\sim 0.16$  km/Ma at  $\sim 34$  Ma due to the onset of the Europe-Adria collision. In contrast, zircon fission track ages from units at a lower structural level and near the indenter indicate cooling during the Eocene; apatite fission track ages cluster at  $\sim 15$  Ma. These units were rapidly exhumed ( $\sim 0.76$  km/Ma) from  $\sim 44$  to  $\sim 39$  Ma during an Eocene phase of shortening prior to the Europe-Adria collision. After slow exhumation ( $\sim 0.13$  km/Ma) between  $\sim 39$  and  $\sim 18$  Ma, the exhumation rate increased to  $\sim 0.27$  km/Ma in the wake of Miocene escape tectonics in the Eastern Alps.

### 1. Introduction

The formation of orogenic belts like the Himalayas and the European Alps commonly starts with the closure of an ocean basin followed by subduction of a passive continental margin and the collision of two continents (Burchfiel, 1982; Butler, 1986; Schmid et al., 1996; van den Beukel, 1992). The convergence between the two continents causes shortening, crustal thickening and isostatic uplift, with the resulting topography being the target of erosional denudation, which, in turn, leads to the exhumation of rocks (Bernet et al., 2009; Hurford, 1991; Molnar & Lyon-Caen, 1988; Rosenberg & Berger, 2009; Stüwe & Barr, 1998). During the subsequent evolution, an orogenic belt may experience syn- or late-orogenic extension by normal faulting and/or lateral extrusion along strike slip faults, with the possible opening of tectonic windows (Dewey, 1988; Frisch, Dunkl, & Kuhlemann, 2000; Mancktelow, 1992; Ratschbacher, Frisch, et al., 1991; Ratschbacher, Merle, et al., 1991; Wallis et al., 1993). Potential reasons for the onset of extension could be a change in lithospheric thickness by the removal of mantle lithosphere or a reduction in compressional stresses transmitted across the plate boundary (Henk, 1997; Molnar et al., 1993), whereas lateral extrusion may be triggered by the development of a retreating subduction boundary in the vicinity of the collision zone (Royden, 1993) or indentation of a weaker plate by a more rigid indenter (Ratschbacher, Merle, et al., 1991; Tapponnier & Molnar, 1976). As a result of crustal extension, rocks may be exhumed by both erosion and tectonic denudation (England & Molnar, 1990; Ring et al., 1999).

As mountain building involves intense ductile and brittle deformation, geological records from earlier orogenic phases are often overprinted and only occasionally preserved. In this respect, the Eastern European Alps represent a remarkable case because here two orogenies that occurred in the Cretaceous and Cenozoic, respectively, are preserved in the geological record (Froitzheim et al., 1994; Kurz & Fritz, 2003; Neubauer et al., 2000; Schmid et al., 1996, 2004). After the closure of the Meliata ocean by E-directed subduction, the Cretaceous orogeny (also

**Validation:** Andreas Wölfler, Andrea Hampel, Ralf Hetzel, István Dunkl

**Visualization:** Andreas Wölfler, Reinhard Wolff, Andrea Hampel

**Writing – original draft:** Andreas Wölfler

**Writing – review & editing:** Andreas Wölfler, Reinhard Wolff, Andrea Hampel, Ralf Hetzel, István Dunkl

referred to as “Eo-Alpine” event) involved intracontinental subduction and led to formation of the Austroalpine nappe stack (Figure 1) (Kurz & Fritz, 2003; Schmid et al., 2008; Schuster et al., 2013). WNW-ward directed nappe stacking was accompanied by top-to-the-ESE extension in the Late Cretaceous (Froitzheim et al., 1997; Kurz & Fritz, 2003; Ratschbacher et al., 1989). After the Cretaceous orogeny, the Eastern Alps experienced a phase of tectonic quiescence without major changes in altitude until the middle Eocene (Dunkl et al., 2005; Oberhauser, 1995; Wagreich & Faupl, 1994). The Cenozoic orogeny started with the closure of the Penninic ocean by SE-directed subduction, which led to the collision between the European and Adriatic Plates (Schmid et al., 1996). In the course of this second orogeny, the Austroalpine nappes were thrusted northwestward over units from the Penninic oceans and the European continental margin (Groß et al., 2020; Liu et al., 2001; Neubauer et al., 2000; Ring et al., 1989). Since the Miocene, the Eastern Alps experienced lateral extrusion to the east and E-W directed extension (Caporali et al., 2009; Frisch, Dunkl, & Kuhlemann, 2000; Ratschbacher, Frisch, et al., 1991; Ratschbacher, Merle, et al., 1991) as well as N-S shortening, crustal thickening and erosion (Rosenberg et al., 2015, 2018).

Although the Austroalpine nappes have a long tectonic record since the Cretaceous, their exhumation history remains poorly resolved, at least partly due to the fact that most thermochronological studies focused on the Cenozoic orogeny. As a consequence, the spatial distribution of the low-temperature thermochronological data, that is, zircon and apatite fission track and (U-Th)/He analyses (ZFT, AFT, ZHe, AHe), is highly irregular in the Eastern Alps, with many data originating from the Tauern Window and its western and southern margins (Figure 2). The Cretaceous cooling history is only captured by a few ZFT ages from the Kreuzeck block located south of the Tauern Window (Dunkl et al., 2003; Wölfler et al., 2008; Wölfler, Dekant, et al., 2015). In regions where the Cretaceous exhumation history might be better preserved, that is, in the Austroalpine units to the west and east of the Tauern Window, considerably fewer cooling ages from only 1–2 thermochronometers are available (Figure 2). West of the Tauern Window, ZFT and AFT ages from the Ötztal nappe range from ca. 99–71 and 62–9 Ma, respectively (Elias, 1998; Fügenshuh et al., 1997; Pomella et al., 2012; Viola et al., 2001). In the Niedere Tauern northeast of the Tauern Window, only AHe and AFT ages are available, which constrain the cooling history since ca. 24 Ma (Hejl, 1997, 1998; Reinecker, 2000; Wölfler et al., 2016). East of the Tauern Window, low-temperature thermochronological data are even sparser, with only a handful of AFT ages (ca. 37–29 Ma) from the Austroalpine units of Gurktal Alps (Hejl, 1997, 1998; Reinecker, 2000). Still farther to the east, AFT ages (ca. 53–31 Ma; Hejl, 1997, 1998) and AHe ages (33–23 Ma, Legrain et al., 2014) were obtained in the Koralpe mountains (Figure 2). East of ca. 14.8°E, van Gelder et al. (2020) obtained ZFT ages of ca. 73–53 Ma and AFT ages of ca. 50–14 Ma along the Mur-Mürz Fault (MMF) system. As a consequence, the cooling and exhumation history of the Austroalpine units east of the Tauern Window and particularly in the Gurktal Alps remains poorly constrained.

Here we present new zircon and apatite fission track and (U-Th)/He data from the Gurktal Alps (Figure 1), including the first ZFT and ZHe ages as well as the first two age-elevation profiles from this region. Located east of the Tauern Window and bounded to the south by the southern border of Alpine Metamorphism (SAM in Figure 1c), the Gurktal Alps expose Austroalpine units from different structural levels and therefore represent a key region for studying the structure and the tectono-metamorphic evolution of the Austroalpine nappe stack since the Eo-Alpine orogeny (Figures 1b and 1c) (e.g., Hoinkes et al., 1999; Krenn et al., 2011; Schuster & Frank, 1999; Schuster et al., 2013; Tollmann, 1977, 1986). However, while the tectono-metamorphic history of the Austroalpine units exposed in the Gurktal Alps has been investigated in some detail (e.g., Hoinkes et al., 1999; Krenn et al., 2011; Rantitsch & Russegger, 2000; Schuster & Frank, 1999; Schuster et al., 2004, 2013; Tollmann, 1977, 1986), their exhumation history since the Eo-Alpine orogeny remains poorly resolved (Figure 2). Based on our thermochronological data set and thermokinematic modeling, we are able to constrain the cooling and exhumation history of the Austroalpine units in the Gurktal Alps in unprecedented detail. In particular, our data show that the exhumation of the miscellaneous Austroalpine units occurred during different tectonic events in the Eastern Alps, depending on the structural position of the individual units within in the nappe stack and relative to the Adriatic indenter. Furthermore, our data provide, for the first time, quantitative constraints for an Eocene phase of enhanced exhumation in the Eastern Alps. This Eocene phase may be related to a period of shortening and relief formation, which preceded the Europe Adria collision (e.g., Dunkl et al., 2005; Neubauer et al., 2000; Wagreich, 2001) and may be correlated with the Blaisun phase of N-S shortening in the eastern Swiss Alps (Froitzheim et al., 1994; Pfiffner, 2009).

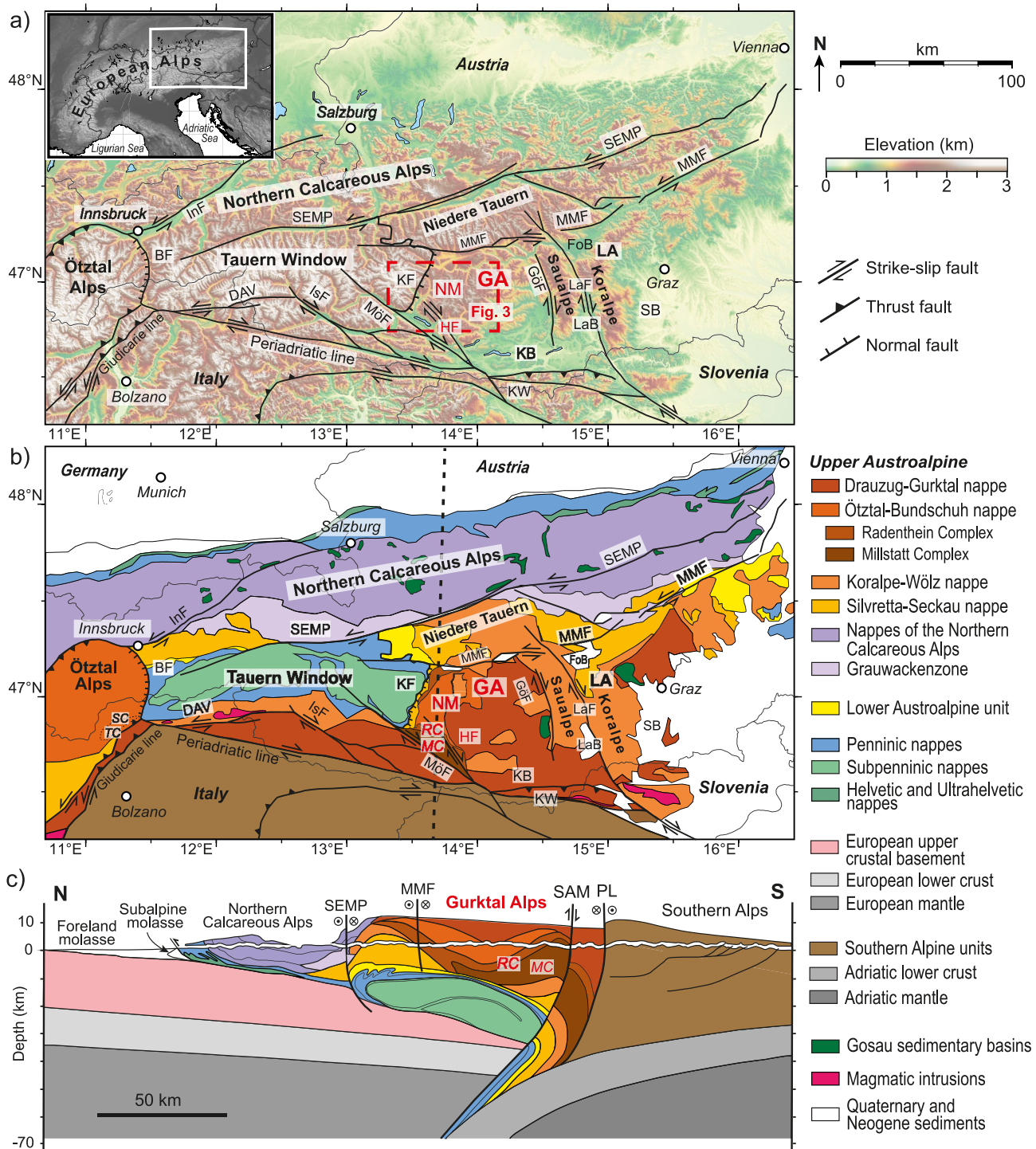


**Figure 1.** Tectonic setting of the Eastern European Alps. (a) Topographic map with major faults (simplified from Linzer et al. (2002), with modifications based on Rosenberg and Schneider (2008) and Ortner et al. (2015)) and sedimentary basins. (b) Map of the major tectonic units (simplified from Schmid et al. (2004), taking into account findings by Krenn et al. (2011) and Klug and Froitzheim (2022)). Abbreviations for regions in the Eastern Alps are GA Gurktal Alps (with NM Nock Mountains), LA Lavanttal Alps, KW Karawanken Mountains. Abbreviations for faults are BF Brenner Fault, DAV Defferegg-Antholz-Vals Fault, GÖF Görttschitztal Fault, HF Hochstuhl Fault, InF Innal Fault, KF Katschberg Fault, LaF Lavanttal Fault, MMF Mur-Mürz Fault, MÖF Mölltal Fault, SEMP Salzach-Ennstal-Puchberg Fault. Abbreviations for sedimentary basins are KB Klagenfurt Basin, LaB Lavanttal Basin and SB Styrian Basin. Other abbreviations are RC Radenthein Complex, MC Millstatt Complex, SC Schneeberg Complex and TC Texel Complex. (c) Cross-section through the Eastern Alps based on Schuster et al. (2013) and Schmid et al. (2004), with modifications that take into account findings by Krenn et al. (2011) and Klug and Froitzheim (2022). For location of profile see panel (b). Abbreviations are PL Periadriatic Line and SAM Southern Border of Alpine Metamorphism (location after Hoinkes et al. (1999) and Schuster et al. (2013)).

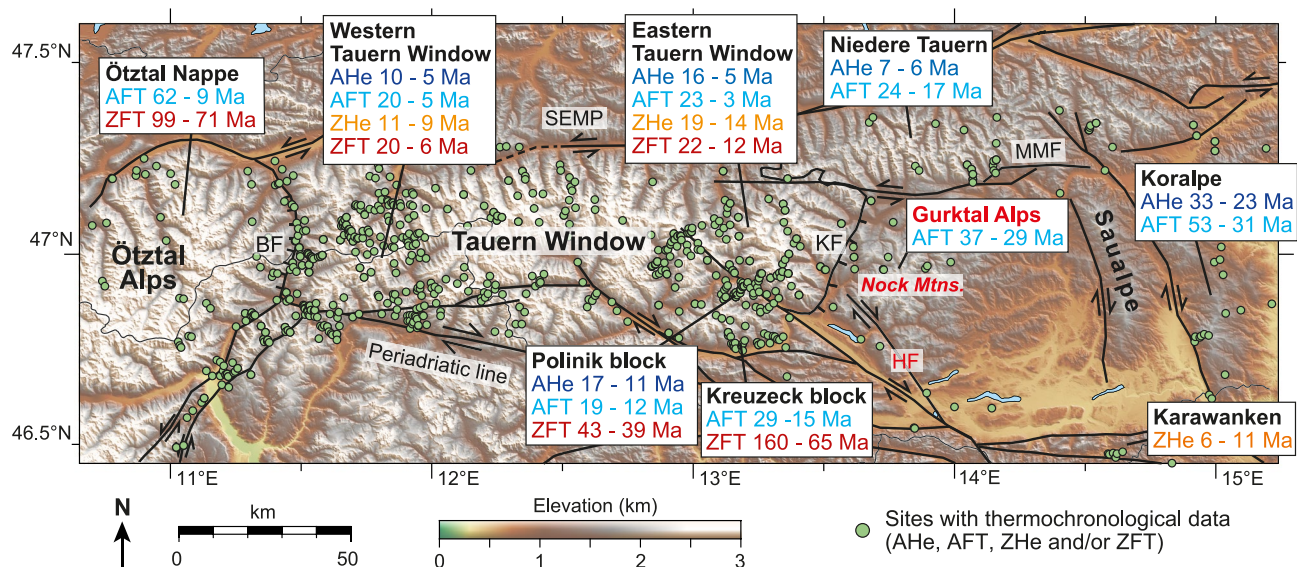


**Figure 2.** Map of the Eastern Alps showing the sites with available thermochronological data and range of cooling ages for regions mentioned in the text. Data are (in alphabetical order) from Bertrand et al. (2017), Coyle (1994), Di Fiore (2013), Dunkl and Demény (1997), Dunkl et al. (2003), Eizenhöfer et al. (2021), Elias (1998), Flisch (1986), Fodor et al. (2008), Foeken et al. (2007), Fügenschuh (1995), Fügenschuh et al. (1997, 2000), Grundmann and Morteani (1985), Heberer et al. (2016), Hejl (1997, 1998), Hejl and Grundmann (1989), Legrain et al. (2014), Mancktelow et al. (2001), Martin et al. (1998), Most (2003), Neubauer et al. (1995), Pomella et al. (2010, 2012), Reinecker (2000), Sachsenhofer et al. (1997), Staufenberg (1987), Steenken et al. (2002), Stöckhert et al. (1999), van Gelder et al. (2020), Viola (2000), Viola et al. (2001, 2003), Wölfler et al. (2008, 2012, 2016); Wölfler, Frisch, et al. (2015), Wölfler, Dekant, et al. (2015), and Wolff et al. (2020, 2021).

## 2. Geological Background

### 2.1. Tectonic Evolution of the Eastern Alps

The Austroalpine nappe stack formed during the Cretaceous orogeny, which involved intracontinental subduction (Kurz & Fritz, 2003; Schmid et al., 2008; Schuster, 2003; Stüwe & Schuster, 2010) and metamorphism that reached peak conditions in the Late Cretaceous (Thöni, 2006; Thöni & Miller, 1996). The Austroalpine nappe stack can be subdivided into Lower and Upper units (Schmid et al., 2004). The Lower Austroalpine unit represents the Adriatic continental margin adjacent to the Piemont-Ligurian ocean and overlies the Penninic nappe stack. The Upper Austroalpine unit comprises several nappes, each of which consists of continental basement and a sedimentary cover originating from the Adriatic Plate (Figures 1b and 1c). The nappe stack formed by WNW-directed thrusting, which migrated westward through time and was followed by top-to-the-ESE normal faulting. In this context, Early Cretaceous thrust faults were overprinted and acted as normal faults during the Late Cretaceous (Froitzheim et al., 1994, 1997; Kurz & Fritz, 2003; Neubauer et al., 1995, 2000; Ratschbacher et al., 1989). This Late Cretaceous extension led to exhumation of high-pressure rocks and the formation of the Gosau sedimentary basins (Figure 1b) (Faupl & Wagreich, 2000; Faupl et al., 1987; Willingshofer et al., 1999).

During the Paleocene and most of the Eocene, the Eastern Alps experienced a period of relative tectonic quiescence without major changes in elevation (Dunkl et al., 2005; Wagreich & Faupl, 1994). The Cenozoic orogeny was triggered by the SE-directed subduction of the Penninic ocean and the passive continental margin of Europe beneath the Adriatic upper plate (Handy et al., 2010, 2015). Subduction of the distal continental margin did not commence before the Early Eocene as indicated by the present of pelagic Eocene sediments in the Penninic units (Neubauer et al., 2000; Schmid et al., 1996, 2013). Between the Early and Late Eocene, the Eastern Alps experienced a phase of shortening, which involved exhumation and relief formation and ended the sedimentation in the Gosau Basins (Dunkl et al., 2005; Faupl & Wagreich, 2000; Fodor et al., 1999; Kázmér et al., 2003; Tollmann, 1986; Wagreich, 2001). The phase of shortening is probably related to the thrusting of Austroalpine nappes over Penninic and Sub-Penninic units (e.g., Liu et al., 2001; Neubauer et al., 2000) and may correlate with the Blaisun phase (ca. 50–35 Ma) of top N-thrusting of Austroalpine and previously accreted Upper Penninic units over structurally lower Penninic units, which has been documented in the eastern Swiss Alps (Froitzheim et al., 1994; Pfiffner, 2009). It may have been during the Blaisun phase that the Austroalpine nappes were internally folded (Figure 1c) (Froitzheim et al., 1994; Pfiffner, 2009). The transition from passive-margin subduction

to continent-continent collision occurred in the Late Eocene (Handy et al., 2010; Neubauer et al., 2000; Rosenberg et al., 2015; Schmid et al., 1996; Süssingh, 1997). The onset of collision at ~35 Ma (Handy et al., 2010) is marked by the development of the Molasse foreland basin (Kuhlemann et al., 2002; Neubauer et al., 2000; Rosenberg et al., 2018; Süssingh, 1997). Parts of the Penninic units experienced high-pressure/low-temperature metamorphism (Frank et al., 1987; Groß et al., 2020; Oberhänsli, 2004). In the Tauern Window, the age of the high-pressure metamorphism is inferred to be 44–37 Ma, based on  $^{40}\text{Ar}/^{39}\text{Ar}$  ages of phengite and Na-amphibole (Dingeldey et al., 1997; Kurz et al., 2008; Ratschbacher et al., 2004). Younger ages of ~33–31 Ma for the high-pressure metamorphism have been derived from multimineral Rb/Sr internal isochron ages (Glödny et al., 2005) and a Lu-Hf isochron age for garnet (Nagel et al., 2013).  $^{40}\text{Ar}/^{39}\text{Ar}$  ages that fall between these time intervals (i.e., ~36–32 Ma) were obtained by Zimmermann et al. (1994) from several Penninic units. During the Oligocene, the Eastern Alps were also affected by magmatic events (e.g., Deutsch, 1984; Laubscher, 1983; Müller et al., 2000; Romer & Siegesmund, 2003), possibly related to the breakoff of the subducted slab (von Blanckenburg & Davies, 1995). The ascent of magma and the emplacement of plutons was facilitated by transpressive deformation along the Periadriatic Fault system (Rosenberg, 2004).

Since the Miocene, the Eastern Alps have experienced lateral extrusion, which encompasses extensional collapse and tectonic escape accommodated by normal faults and conjugate sets of strike-slip faults, respectively (Ratschbacher et al., 1989; Ratschbacher, Frisch, et al., 1991; Ratschbacher, Merle, et al., 1991). The region of the Eastern Alps affected by lateral extrusion is bounded by the Innal Fault, the Salzach-Ennstal-Mariazell-Puchberg Fault system (SEMP) and the MMF system to the north and the Periadriatic Fault system to the south (Figure 1a). Lateral extrusion is driven by the indentation of the Eastern Alps by the South Alpine units (Figure 1b), which caused N-S shortening and led to crustal-scale folding and thrust faulting (Rosenberg et al., 2015, 2018), including the formation of deep-seated thrust faults such as the S-dipping Tauern ramp (e.g., Gebrände et al., 2002; Lüschen et al., 2004). In concert, lateral extrusion, E-W extension, N-S shortening and erosion led to the formation of the Tauern Window, with the result that formerly related Austroalpine units are now located east and west of the Tauern Window and Penninic and Subpenninic units are exposed in the Tauern Window (Figure 1) (Behrmann, 1988; Frisch, Dunkl, & Kuhlemann, 2000; Fügenschuh et al., 1997; Genser & Neubauer, 1989; Krenn et al., 2011; Neubauer et al., 1999; Ratschbacher, Frisch, et al., 1991; Rosenberg, 2004; Rosenberg & Berger, 2009; Rosenberg et al., 2004, 2015, 2018; Selverstone, 1988; Wolff et al., 2020, 2021). The relative contribution of normal faulting, thrust faulting and erosion to rock exhumation in the Tauern Window is still under debate (Eizenhöfer et al., 2021; Fügenschuh et al., 2012; Rosenberg & Garcia, 2011, 2012; Rosenberg et al., 2018; Wolff et al., 2020, 2021).

## 2.2. Geological Setting of the Study Area

Our study area is located east of the Tauern Window in the Nock Mountains, which form the western part of the Gurktal Alps (Figure 1a). To the north, the Gurktal Alps are bounded by the MMF and to the south by the Mölltal Fault (Figure 1a). Through the southern part of the Nock Mountains runs the NW-SE striking, dextral Hochstuhl Fault, which joins the Mölltal Fault to the south (Figure 1a) (Linzer et al., 2002; Polinski & Eisbacher, 1992).

In the Gurktal Alps, four Upper Austroalpine nappes occur, which are—from structurally highest to lowest level—the Drauzug-Gurktal nappe, the Ötztal-Bundschnuh nappe, the Koralpe-Wölz nappe, and the Silvretta-Seckau nappe (Figures 1 and 3). The Drauzug-Gurktal nappe comprises Early Paleozoic clastic metasediments with intercalated metatuffites and carbonates. As well as Permo-Mesozoic sediments, which form the sedimentary cover of the nappe (Krainer, 1984). The entire nappe was overprinted at sub-greenschist to lower greenschist facies conditions during the Eo-Alpine event (Thöni, 2006). The Ötztal-Bundschnuh nappe consists of a Variscan metamorphic basement, sub-greenschist to greenschist-facies Paleozoic metasediments and Permo-Triassic sediments (Rantitsch & Russegger, 2000). The Koralpe-Wölz nappe comprises Paleozoic metasediments and basement rocks, which experienced high-T/low-P metamorphism in the Permo-Triassic and an Eo-Alpine (100–90 Ma) low-T/high-P metamorphic overprint (Miladinova et al., 2022; Schuster et al., 2004; Thöni, 2006).  $^{40}\text{Ar}/^{39}\text{Ar}$  mineral cooling ages from the Koralpe-Wölz nappe range from 90 to 70 Ma (Dallmeyer et al., 1996; Hoinkes et al., 1999; Thöni, 1999). The structurally lowest nappe, the Silvretta-Seckau nappe, consists of a pre-Alpine basement and minor Carboniferous to Triassic sediments. During the Eo-Alpine event, this nappe experienced greenschist-facies conditions (Pfingstl et al., 2015; Schuster et al., 2013).

In addition to the four nappes described in the previous paragraph, two complexes with different metamorphic histories occur in the southern part of our study area: the Radenthein Complex and the Millstatt Complex (RC and MC in Figure 3a). The Radenthein Complex has a monometamorphic history, as indicated by a single phase

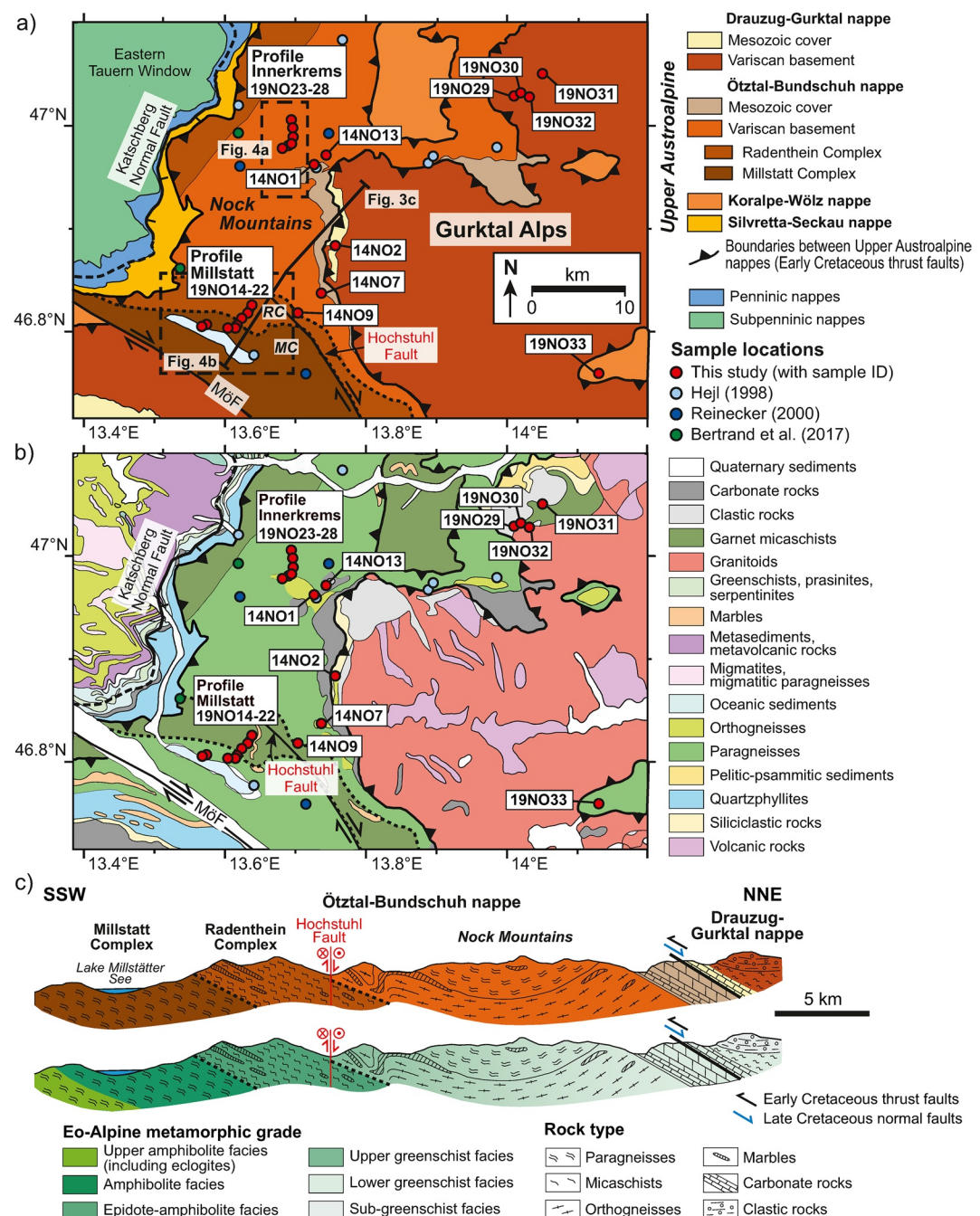


**Figure 3.** Overview of the study area. (a) Map showing the Austroalpine nappes of the Gurktal Alps (modified from Schmid et al. (2013) and Iglseder (2019)). The Radenthein and Millstatt Complexes (RC, MC) are shown based on Krenn et al. (2011) and Klug and Froitzheim (2022). (b) Geological map of the study area. Surface traces of faults after Schmid et al. (2013), Scharf et al. (2013), and Bertrand et al. (2017). Color-filled circles indicate sampling sites of this and earlier thermochronological studies. (c) Cross-sections showing the structural position and the eo-Alpine metamorphic grade of the Drauzug-Gurktal nappe, the Ötztal-Bundschuh nappe and the Radenthein and Millstatt Complexes (after Schuster et al. (2013); taking into account findings by Klug and Froitzheim (2022)). Thick solid black line marks boundary between Drauzug-Gurktal and Ötztal-Bundschuh nappes; thick dashed black line marks boundaries of Radenthein and Millstatt Complexes. Thin solid black line marks the Hochstuhl fault. For location of cross-section see panel (a).

of garnet growth (Krenn et al., 2011). This Eo-Alpine metamorphic event at ~100 Ma (Schuster & Frank, 1999) reached peak temperatures of 550–650°C and pressures of 0.6–1.0 GPa (Kaindl & Abart, 2002; Koroknai et al., 1999). In contrast, the Millstatt Complex is polymetamorphic and contains garnet with Variscan core

**Table 1***Location, Lithology, and Structural Position of Samples for Low-Temperature Thermochronology*

Sample	Latitude (°N) (WGS 84)	Longitude (°E) (WGS 84)	Elevation (m)	Lithology	Structural position	Thermochronometers applied
14NO1	46.9622	13.7278	1,572	Orthogneiss	Ötztal-Bundschuh nappe system	AHe, AFT
14NO2	46.8836	13.7564	2,050	Paragneiss	Ötztal-Bundschuh nappe system	AFT
14NO7	46.8375	13.7369	1,881	Orthogneiss	Ötztal-Bundschuh nappe system	AFT
14NO9	46.8183	13.7036	859	Paragneiss	Ötztal-Bundschuh nappe system	AFT
14NO13	46.9717	13.7436	1,531	Paragneiss	Ötztal-Bundschuh nappe system	AHe, AFT, ZHe, ZFT
19NO14	46.8258	13.6383	2,042	Micaschist	Radenthein Complex	AFT, ZFT
19NO15	46.8215	13.6350	1,945	Micaschist	Radenthein Complex	AFT, ZFT
19NO16	46.8181	13.6322	1,828	Micaschist	Radenthein Complex	AFT, ZFT
19NO17	46.8129	13.6238	1,540	Paragneiss	Millstatt Complex	AFT, ZFT
19NO18	46.8063	13.6171	1,232	Paragneiss	Millstatt Complex	AFT, ZFT
19NO19	46.8036	13.6147	1,061	Paragneiss	Millstatt Complex	AFT, ZHe, ZFT
19NO20	46.8036	13.6042	880	Paragneiss	Millstatt Complex	AFT, ZFT
19NO21	46.8070	13.5740	696	Paragneiss	Millstatt Complex	AHe, AFT, ZFT
19NO22	46.8050	13.5671	624	Paragneiss	Millstatt Complex	AFT, ZFT
19NO23	46.0058	13.6942	2,211	Paragneiss	Ötztal-Bundschuh nappe system	AHe, AFT, ZHe, ZFT
19NO24	46.9982	13.6962	2,030	Paragneiss	Ötztal-Bundschuh nappe system	AFT, ZHe, ZFT
19NO25	46.9892	13.6966	1,800	Paragneiss	Ötztal-Bundschuh nappe system	AFT, ZFT
19NO26	46.9827	13.6943	1,563	Paragneiss	Ötztal-Bundschuh nappe system	AFT, ZHe, ZFT
19NO27	46.9809	13.6903	1,421	Orthogneiss	Ötztal-Bundschuh nappe system	AHe, AFT, ZFT
19NO28	46.9782	13.6814	1,294	Orthogneiss	Ötztal-Bundschuh nappe system	AHe, AFT, ZHe, ZFT
19NO29	47.0289	14.0101	1,161	Micaschist	Drauzug-Gurktal nappe system	AFT, ZFT
19NO30	47.0321	14.0198	1,451	Micaschist	Drauzug-Gurktal nappe system	AFT, ZFT
19NO31	47.0506	14.0505	2,118	Micaschist	Drauzug-Gurktal nappe system	AFT, ZHe, ZFT
19NO32	47.0281	14.0317	1,683	Micaschist	Drauzug-Gurktal nappe system	AFT, ZHe, ZFT
19NO33	46.7594	14.1304	710	Paragneiss	Drauzug-Gurktal nappe system	AFT, ZHe, ZFT

and Eo-Alpine rim. Peak metamorphic conditions reached  $630 \pm 20^\circ\text{C}$  and  $\sim 1.4 \text{ GPa}$  during the Eo-Alpine event (Hoinkes et al., 1999). Notably, the Radenthein and Millstatt Complexes show the same metamorphic characteristics as the Schneeberg and Texel complexes west of the Tauern Window, respectively (Figure 1b) (Krenn et al., 2011). The latter were long regarded as part of the Koralpe-Wölz nappe (e.g., Krenn et al., 2011; Schmid et al., 2004; Sörla et al., 2005). A recent study, however, demonstrated that the Schneeberg and Texel Complexes form part of the Ötztal-Bundschuh nappe (Klug & Froitzheim, 2022). Hence, the Millstatt and Radenthein Complexes in our study may also belong to the Ötztal-Bundschuh nappe.

### 3. Sampling Strategy and Analytical Methods

We collected a total of 25 samples in the Gurktal Alps, including 6 and 9 samples along two elevation profiles in the center of the Nock Mountains (profile Innerkrems) and their southern part (profile Millstatt), respectively (Figure 3). The sampled rock types are orthogneisses and paragneisses from the Ötztal-Bundschuh nappe, and micaschists and paragneisses from the Drauzug-Gurktal nappe and the Millstatt and Radenthein Complexes (Table 1; Figure 3). To constrain the cooling history of these samples between  $<300^\circ\text{C}$  and near-surface temperatures, we applied the four thermochronometers ZFT, ZHe, AFT, and AHe whenever the samples yielded zircon and apatite crystals of sufficient quality for the respective method (see below). Taken together, the samples yielded 25 AFT ages, 21 ZFT ages, 9 ZHe ages, and 6 AHe ages (Table 1).

**Table 2**  
*Results of Zircon Fission Track Analyses*

Sample	Number of grains	ps	Ns	pi	Ni	pd	Nd	P( $\chi^2$ ) (%)	Central age $\pm 1\sigma$ (Ma)	U (ppm)
<b>14NO13</b>	15	31.444	283	14.222	128	6.931	1,146	57.66	<b>93.4 <math>\pm</math> 12.9</b>	125
<b>19NO14</b>	20	32.155	452	30.590	430	6.797	1,974	98.12	<b>46.2 <math>\pm</math> 4.4</b>	149
<b>19NO15</b>	20	28.959	464	27.461	440	6.452	1,974	100.00	<b>44.0 <math>\pm</math> 4.2</b>	129
<b>19NO16</b>	20	32.045	441	30.737	423	6.436	1,974	97.44	<b>43.4 <math>\pm</math> 4.2</b>	153
<b>19NO17</b>	20	28.430	422	28.430	422	6.420	1,974	99.01	<b>41.4 <math>\pm</math> 4.0</b>	137
<b>19NO18</b>	20	29.046	434	29.649	443	6.404	1,974	100.00	<b>40.5 <math>\pm</math> 3.9</b>	136
<b>19NO19</b>	20	32.553	448	36.841	507	6.838	1,974	97.01	<b>39.1 <math>\pm</math> 3.7</b>	218
<b>19NO20</b>	20	42.944	553	45.817	590	6.372	1,974	80.48	<b>38.6 <math>\pm</math> 3.6</b>	220
<b>19NO21</b>	20	38.996	552	40.762	577	6.356	1,974	99.95	<b>39.3 <math>\pm</math> 3.5</b>	196
<b>19NO22</b>	20	40.985	560	43.692	597	6.340	1,974	49.73	<b>38.4 <math>\pm</math> 3.5</b>	227
<b>19NO23</b>	20	76.877	1,126	35.435	519	6.308	1,974	99.40	<b>88.3 <math>\pm</math> 7.6</b>	170
<b>19NO24</b>	18	80.553	1,164	38.962	563	6.307	1,974	91.39	<b>84.0 <math>\pm</math> 8.0</b>	185
<b>19NO25</b>	20	86.624	1,124	39.921	518	6.299	1,974	99.99	<b>88.0 <math>\pm</math> 7.6</b>	193
<b>19NO26</b>	20	90.900	1,108	44.219	539	6.292	1,974	99.92	<b>83.3 <math>\pm</math> 7.1</b>	215
<b>19NO27</b>	20	103.624	1,039	48.072	482	6.276	1,974	99.98	<b>87.1 <math>\pm</math> 7.6</b>	245
<b>19NO28</b>	20	81.384	1,072	36.364	479	6.260	1,974	96.84	<b>90.2 <math>\pm</math> 7.9</b>	174
<b>19NO29</b>	20	117.408	981	53.976	451	6.266	1,974	100.00	<b>87.5 <math>\pm</math> 7.7</b>	292
<b>19NO30</b>	20	95.234	1,217	45.465	581	6.229	1,974	100.00	<b>84.0 <math>\pm</math> 7.1</b>	235
<b>19NO31</b>	20	32.461	1,270	52.807	548	6.181	1,974	57.33	<b>92.2 <math>\pm</math> 7.8</b>	390
<b>19NO32</b>	20	126.566	1,381	57.280	625	6.197	1,974	99.62	<b>88.2 <math>\pm</math> 7.3</b>	313
<b>19NO33</b>	20	94.711	1,201	44.714	567	6.213	1,974	64.25	<b>90.9 <math>\pm</math> 7.7</b>	223

Note. ps (pi) is the spontaneous (induced) track density ( $10^5$  tracks/cm $^2$ ); Ns (Ni) is the number of counted spontaneous (induced) tracks; pd is the dosimeter track density ( $10^5$  tracks/cm $^2$ ); Nd is the number of tracks counted on the dosimeter; P( $\chi^2$ ) is the probability of obtaining a Chi-square value ( $\chi^2$ ) for n degrees of freedom (where n is the number of crystals minus 1); ages were calculated using the zeta calibration method (Hurford & Green, 1983), glass dosimeter IRMM541, and a zeta value of  $109 \pm 3$  a/cm $^2$  determined with the Fish Canyon Tuff zircon standard. Sample IDs and measured thermochronological ages are shown in bold for an easy correlation.

### 3.1. Zircon and Apatite Fission-Track Analysis

For fission track analysis, zircon and apatite grains were separated using conventional magnetic and heavy liquid separation techniques and embedded in PDA Teflon™ and epoxy, respectively, ground and polished. Zircon mounts were etched in a KOH-NaOH eutectic melt at 215°C (Zaun & Wagner, 1985); the apatites were etched with 5 M HNO<sub>3</sub> for 20 s at 21°C (Donelick et al., 1999). The samples were irradiated with thermal neutrons at the SCK CEN Belgian Nuclear Research Centre in Mol. Fission track counting was carried out with an Olympus BX-51 microscope under 1,000 $\times$  magnification at the Institute of Geology in Hannover. We used the external detector method (Gleadlow, 1981) with uranium-free muscovite sheets and the zeta calibration approach (e.g., Hurford & Green, 1983; Naeser, 1978) with dosimeter glasses IRMM-540R and IRMM-541 and Durango apatite and Fish Canyon zircon age standards. For the assessment of annealing kinetics in apatites we used Dpar values (mean diameter of etch figures on prismatic surfaces of apatite parallel to the crystallographic c-axis) (Burtner et al., 1994). The mean track lengths from horizontal confined tracks were corrected for c-axis orientation (Donelick et al., 1999). Fission track ages were calculated with the Trackkey software version 4.2 (Dunkl, 2002) and are reported in Tables 2 and 3.

### 3.2. Zircon and Apatite (U-Th)/He Analysis

For (U-Th)/He dating, zircon and apatite crystals were hand-picked using a stereo- and polarizing microscope and selected under 200 $\times$  magnification following the selection criteria of Farley (2002) and Reiners (2005).

**Table 3**  
*Results of Apatite Fission Track Analyses*

Sample	Number of grains	ps	Ns	pi	Ni	pd	Nd	P( $\chi^2$ ) (%)	Central age $\pm 1\sigma$ (Ma)	U (ppm)	Mean track length ( $\mu\text{m}$ )	SD ( $\mu\text{m}$ )	Number of track lengths measured	Dpar ( $\mu\text{m}$ )
<b>14NO1</b>	25	2.085	59	5.583	158	7.7568	2,658	99.10	<b>36.8 <math>\pm</math> 5.8</b>	10	14.10	1.20	50	1.71
<b>14NO2</b>	25	1.624	57	4.501	158	7.7579	2,658	100.00	<b>35.6 <math>\pm</math> 5.7</b>	8	14.0	1.31	60	1.62
<b>14NO7</b>	25	1.812	54	5.000	149	7.7571	2,658	99.54	<b>35.8 <math>\pm</math> 5.9</b>	9	13.9	1.01	64	1.52
<b>14NO9</b>	25	2.090	65	6.174	192	7.7575	2,658	99.72	<b>33.4 <math>\pm</math> 5.0</b>	11	13.9	1.32	55	1.63
<b>14NO13</b>	25	1.993	73	5.898	216	7.7582	2,658	99.81	<b>33.4 <math>\pm</math> 4.5</b>	10	14.1	1.22	50	1.61
<b>19NO14</b>	25	2.570	71	11.440	316	7.412	2,581	97.11	<b>18.9 <math>\pm</math> 2.7</b>	22	13.86	0.63	21	2.12
<b>19NO15</b>	25	1.497	54	7.068	255	7.365	2,581	100.00	<b>17.7 <math>\pm</math> 2.9</b>	13	13.60	0.56	12	1.87
<b>19NO16</b>	25	1.769	60	8.817	299	7.322	2,581	100.00	<b>16.6 <math>\pm</math> 2.6</b>	17	13.59	0.55	11	1.73
<b>19NO17</b>	25	1.523	47	8.002	247	7.277	2,581	99.13	<b>15.7 <math>\pm</math> 2.7</b>	16	13.66	0.65	17	1.90
<b>19NO18</b>	25	1.824	59	9.987	323	7.232	2,581	92.81	<b>15.0 <math>\pm</math> 2.3</b>	20	13.70	0.66	22	1.79
<b>19NO19</b>	25	1.784	47	9.983	263	7.190	2,581	97.12	<b>14.6 <math>\pm</math> 2.5</b>	20	13.75	1.09	18	1.83
<b>19NO20</b>	25	1.495	46	8.645	266	7.142	2,581	100.00	<b>14.0 <math>\pm</math> 2.4</b>	18	13.70	0.62	15	1.84
<b>19NO21</b>	25	1.149	42	6.673	244	7.097	2,581	99.96	<b>13.8 <math>\pm</math> 2.5</b>	13	13.78	0.64	27	2.15
<b>19NO22</b>	25	1.163	36	6.847	212	7.052	2,581	75.39	<b>13.6 <math>\pm</math> 2.6</b>	14	13.79	0.49	12	1.81
<b>19NO23</b>	25	2.184	70	5.211	167	7.007	2,581	100.00	<b>33.2 <math>\pm</math> 5.2</b>	11	13.63	0.88	20	1.68
<b>19NO24</b>	25	1.827	58	4.346	138	6.962	2,581	92.16	<b>33.1 <math>\pm</math> 5.6</b>	9	13.61	0.92	15	1.67
<b>19NO25</b>	25	1.876	64	4.573	156	6.917	2,581	100.00	<b>32.1 <math>\pm</math> 5.2</b>	10	13.76	0.68	25	1.76
<b>19NO26</b>	25	2.199	67	5.612	171	6.873	2,581	99.56	<b>30.5 <math>\pm</math> 4.8</b>	12	13.61	0.67	12	1.79
<b>19NO27</b>	25	1.690	53	4.305	135	6.828	2,581	99.22	<b>30.3 <math>\pm</math> 5.3</b>	21	13.77	0.53	33	1.93
<b>19NO28</b>	25	2.078	57	5.542	152	6.783	2,581	96.56	<b>28.8 <math>\pm</math> 4.8</b>	9	13.51	1.07	18	1.80
<b>19NO29</b>	25	1.888	62	5.208	171	7.783	2,581	100.00	<b>27.7 <math>\pm</math> 4.4</b>	11	13.65	0.52	20	1.83
<b>19NO30</b>	25	1.658	59	4.075	145	6.693	2,581	100.00	<b>30.8 <math>\pm</math> 5.1</b>	12	13.65	0.61	21	1.79
<b>19NO31</b>	25	1.802	59	4.002	131	6.558	2,581	99.23	<b>33.4 <math>\pm</math> 5.6</b>	8	13.84	0.50	20	1.87
<b>19NO32</b>	25	1.868	56	4.303	129	6.603	2,581	99.98	<b>32.4 <math>\pm</math> 5.6</b>	9	13.66	0.69	28	1.89
<b>19NO33</b>	25	1.759	51	4.621	134	6.648	2,581	85.49	<b>28.6 <math>\pm</math> 5.0</b>	9	13.68	0.43	23	1.94

Note. ps (pi) is the spontaneous (induced) track density ( $10^5$  tracks/cm $^2$ ); Ns (Ni) is the number of counted spontaneous (induced) tracks; pd is the dosimeter track density ( $10^5$  tracks/cm $^2$ ); Nd is the number of tracks counted on the dosimeter; P( $\chi^2$ ) is the probability of obtaining Chi-square value ( $\chi^2$ ) for  $n$  degrees of freedom (where  $n$  is the number of crystals minus 1); ages were calculated using the zeta calibration method (Hurford & Green, 1983), glass dosimeter IRMM540, and a zeta value of  $226 \pm 13$  a/cm $^2$  determined with the Durango apatite standard. Sample IDs and measured thermochronological ages are shown in bold for an easy correlation.

The dimensions of the selected crystals were measured to determine alpha-ejection correction factors (Farley et al., 1996). Single crystals were loaded into pre-cleaned Pt tubes for He analysis, which was carried out at the Gööochron Laboratory at the University of Göttingen (Germany). Extraction of helium from the crystals was performed by heating the encapsulated grain in vacuum using an IR laser. The extracted gas was purified by a SAES Ti-Zr getter and the He content was measured by a Hiden Hal-3F/PIC triple-filter quadrupole mass spectrometer. For measurements of the alpha-emitting elements U, Th, and Sm, the crystals were dissolved and spiked with calibrated  $^{233}\text{U}$  and  $^{230}\text{Th}$  solutions. Zircons were dissolved in Teflon bombs with 48% HF and 65% HNO<sub>3</sub> at 220°C for 5 days. Apatites were dissolved in 2% ultrapure HNO<sub>3</sub> (+0.05% HF) in an ultrasonic bath. The actinide elements, Sm, Zr, Ca and the REE concentrations were measured by inductively coupled plasma mass spectrometry using the isotope-dilution method with a Perkin Elmer Elan DRC II system equipped with an APEX microflow nebulizer and with an iCAP Q ICP-MS. Errors for the single-grain ZHe and AHe analyses are attributed to uncertainties in the He, U, Th, and Sm measurements and the estimated uncertainty of the ejection correction (Ft) factor. The ZHe and AHe ages were calculated as unweighted mean ages from the single-grain ages of each sample and are reported in Tables 4 and 5 with an uncertainty of two standard errors.

**Table 4**  
*Results of Zircon (U-Th)/He Analyses*

Sample	Aliq.	He			U			Th			Sm			Ejection correction	Uncorr. age (Ma)	Ft-corr. age (Ma)	$2\sigma$ (Ma)	Sample age (Ma)	$2\text{se}$ (Ma)
		Vol. ( $10^{-9} \text{ cm}^3$ )	$1\sigma$ (%)	Mass (ng)	Conc. (ppm)	Mass $1\sigma$ (ng)	Conc. (%)	Th/U ratio	Mass $1\sigma$ (ng)	Conc. (ppm)	Mass $1\sigma$ (ng)	Conc. (%)	Mass $1\sigma$ (ng)	Conc. (%)					
<b>14N013</b>	#1	8.637	0.8	0.985	1.8	212	0.415	2.4	89	0.42	0.010	16.3	3	0.75	65.7	<b>87.6</b>	7.3	<b>85.6</b>	<b>2.9</b>
	#2	6.527	0.8	0.734	1.8	152	0.390	2.4	81	0.53	0.016	13.9	3	0.78	65.1	<b>83.5</b>	6.3		
<b>19N019</b>	#1	0.440	1.1	0.237	2.0	74	0.042	2.6	13	0.2	0.006	2.9	2	0.67	14.7	<b>21.9</b>	2.4	<b>23.1</b>	<b>1.4</b>
	#2	1.050	1.1	0.490	1.9	188	0.166	2.4	64	0.3	0.011	2.9	4	0.64	16.5	<b>25.8</b>	3.0		
<b>19N023</b>	#3	1.520	1.1	0.844	1.8	251	0.055	2.5	16	0.1	0.004	2.9	1	0.68	14.7	<b>21.5</b>	2.3		
	#1	2.280	1.9	0.342	1.9	48	0.353	2.4	49	1.0	0.010	2.9	1	0.77	44.6	<b>57.9</b>	4.9	<b>65.5</b>	<b>5.8</b>
<b>19N024</b>	#2	3.090	1.9	0.462	1.8	35	0.207	2.4	16	0.4	0.021	2.9	2	0.81	50.1	<b>61.8</b>	4.7		
	#3	10.150	1.9	1.328	1.8	205	0.817	2.4	126	0.6	0.014	2.9	2	0.72	55.4	<b>76.9</b>	7.5		
<b>19N026</b>	#1	3.450	1.9	0.539	1.8	80	0.221	2.4	33	0.4	0.006	2.8	1	0.76	48.4	<b>63.7</b>	5.6	<b>64.6</b>	<b>1.3</b>
	#2	9.321	1.9	1.317	1.8	120	0.584	2.4	53	0.4	0.027	2.9	2	0.81	53.1	<b>65.6</b>	5.0		
<b>19N027</b>	#1	3.040	1.9	0.534	1.8	65	0.655	2.4	80	1.2	0.035	2.9	4	0.79	36.8	<b>46.5</b>	3.7	<b>60.1</b>	<b>6.8</b>
	#2	9.300	1.9	1.222	1.8	137	0.812	2.4	91	0.7	0.027	2.9	3	0.80	54.6	<b>68.3</b>	5.3		
<b>19N028</b>	#3	8.670	1.9	1.260	1.8	123	0.551	2.4	54	0.4	0.057	2.9	6	0.79	51.7	<b>65.4</b>	5.2		
	#1	0.060	3.6	0.021	9.8	11	0.020	2.8	11	1.0	0.629	2.9	344	0.78	16.2	20.8	3.4	<b>59.7</b>	<b>7.0</b>
<b>19N031</b>	#2	8.978	1.9	1.869	1.8	408	0.181	2.4	40	0.1	0.029	2.9	6	0.65	38.8	<b>59.7</b>	7.0		
	#1	17.470	1.9	2.379	1.8	418	0.520	2.4	91	0.2	0.020	2.9	3	0.73	57.7	<b>79.1</b>	7.5	<b>74.6</b>	<b>6.4</b>
<b>19N032</b>	#2	8.750	1.9	1.373	1.8	291	1.264	2.4	56	0.2	0.008	2.9	2	0.72	50.4	<b>70.0</b>	6.8		
	#1	13.860	0.9	1.671	1.8	220	0.773	2.4	102	0.5	0.025	4.6	3	0.79	62.0	<b>78.4</b>	5.7	<b>78.4</b>	<b>2.2</b>
<b>19N033</b>	#2	8.430	0.9	1.064	1.8	104	0.450	2.4	44	0.4	0.030	4.6	3	0.80	59.6	<b>74.5</b>	5.2		
	#3	171.840	0.9	18.257	1.8	368	5.733	2.4	115	0.3	0.195	4.6	4	0.88	72.4	<b>82.3</b>	4.2		
<b>19N034</b>	#1	7.010	1.9	0.938	1.8	320	0.129	2.5	44	0.1	0.038	4.6	13	0.73	59.7	<b>81.8</b>	7.8	<b>82.5</b>	<b>0.5</b>
	#2	10.550	1.9	1.307	1.8	345	0.525	2.4	139	1.4	0.026	4.6	7	0.73	61.0	<b>83.6</b>	7.9		
<b>19N035</b>	#3	11.910	1.9	1.567	1.8	464	0.118	2.5	35	0.1	0.011	4.6	3	0.75	61.6	<b>82.2</b>	7.4		
	#1	4.030	1.9	0.582	1.8	84	0.203	2.4	29	0.3	0.041	2.9	6	0.82	53.0	<b>64.7</b>	4.8	<b>73.5</b>	<b>4.4</b>
<b>19N036</b>	#2	6.620	1.9	0.961	1.8	393	0.126	2.4	51	0.1	0.005	4.6	2	0.71	55.2	<b>77.8</b>	7.8		
	#3	36.670	1.9	4.546	1.8	308	0.822	2.4	56	0.2	0.033	4.6	2	0.82	63.9	<b>77.9</b>	5.7		

Note. Ejection correction (Ft): correction factor for alpha-ejection (according to Farley et al. (1996) and Hourigan et al. (2005)). Uncertainty of the single-grain ages includes both the analytical uncertainty and the estimated uncertainty of the ejection correction. Sample age (2se standard error) is the unweighted average age of all Ft-corrected (U-Th)/He ages. Results from aliquots written in italics are not considered in the calculation of the sample age. Sample IDs and measured thermochronological ages are shown in bold for an easy correlation.

**Table 5**  
*Results of Apatite (U-Th)/He Analyses*

Sample	Aliq.	He			U			Th			Sm								
		Vol. ( $10^{-9}$ cm $^3$ )	$1\sigma$ (%)	Mass (ng)	$1\sigma$ (%)	Conc. (ppm)	Mass (ng)	$1\sigma$ (%)	Conc. (ppm)	Th/U ratio	Mass (ng)	$1\sigma$ (%)	Conc. (ppm)	Ejection correction	Uncorr. age (Ma)	Ft-corr. age (Ma)	$2\sigma$ (Ma)	Sample age (Ma)	$2\sigma$ (Ma)
<b>14NO1</b>	#1	0.094	1.9	0.033	2.4	16.7	0.014	3.1	6.9	0.41	0.197	7.2	99	0.65	20.5	<b>31.6</b>	3.8	<b>35.1</b>	<b>5.1</b>
	#2	0.123	1.7	0.034	2.4	16.5	0.003	5.4	1.2	0.08	0.169	7.7	81	0.72	27.9	<b>38.7</b>	3.9		
<b>14NO13</b>	#1	0.181	1.4	0.056	2.1	19.0	0.005	3.8	1.8	0.09	0.264	6.9	91	0.76	25.4	<b>33.4</b>	2.9	<b>31.3</b>	<b>3.0</b>
	#2	0.199	1.4	0.066	2.0	14.5	0.001	25.6	0.2	0.01	0.417	6.5	92	0.81	23.6	<b>29.4</b>	2.1		
<b>19NO21</b>	#1	0.905	2.0	0.634	1.8	58.3	0.030	2.5	2.8	0.1	3.044	2.8	280	0.79	11.3	<b>14.2</b>	1.2	<b>12.7</b>	<b>2.2</b>
	#2	0.464	2.1	0.426	1.8	86.7	0.043	2.5	8.7	0.1	1.407	2.8	286	0.77	8.6	<b>11.1</b>	1.0		
<b>19NO23</b>	#1	0.190	2.3	0.054	2.0	11.7	0.003	7.6	0.7	0.1	0.453	2.8	99	0.76	27.0	<b>35.5</b>	3.3	<b>35.5</b>	<b>3.3</b>
	#2	0.261	2.1	0.057	2.0	14.1	0.006	2.7	1.5	0.1	0.382	2.8	95	0.75	35.0	<b>46.6</b>	4.4		
<b>19NO27</b>	#1	0.092	2.5	0.018	3.5	5	0.037	2.6	10.6	2.1	0.415	2.8	118	0.77	25.9	<b>33.6</b>	3.2	<b>25.1</b>	<b>4.3</b>
	#2	0.048	4.0	0.018	3.7	7	0.018	3.0	6.9	1.0	0.522	2.8	194	0.70	15.0	<b>21.4</b>	2.8		
<b>19NO28</b>	#3	0.068	3.4	0.027	2.8	6	0.027	2.8	6.0	1.0	0.797	2.8	173	0.71	14.3	<b>20.2</b>	2.4		
	#1	0.041	3.7	0.011	5.2	6.2	0.019	2.9	10.4	1.7	0.418	2.8	231	0.67	18.3	<b>27.3</b>	3.8	<b>27.3</b>	<b>3.8</b>

Note: Ejection correction (F); correction factor for alpha-ejection (according to Farley et al. (1996)). Uncertainty of the single-grain ages includes both the analytical uncertainty and the estimated uncertainty of the ejection correction. Sample age ( $2\sigma$  standard error) is the unweighted average age of all Ft-corrected (U-Th)/He ages. Results from aliquots written in italics are not considered in the calculation of the sample age. Sample IDs and measured thermochronological ages are shown in bold for an easy correlation.

**Table 6**  
*Parameters of PECUBE Model*

Model dimensions: length, width, thickness	12 km, 12 km, and 70 km
Temperature at base of model	800°C
Temperature at top of model	2–10°C
Radiogenic heat production	$4.0 \times 10^{-6} \text{ W/m}^3$
E-folding depth of heat production	20 km
Thermal diffusivity	$1 \times 10^{-6} \text{ m}^2/\text{s}$

### 3.3. Thermokinematic Modeling

To extract detailed information on the exhumation history from the Innerkrems and Millstatt elevation profiles, we used the thermokinematic finite element code PECUBE version 4.2 (Braun et al., 2012). By solving the three-dimensional heat-transport equation, PECUBE calculates time-temperature paths during exhumation and computes the resulting thermochronological ages. PECUBE can be used for both forward and inverse modeling. In contrast to thermal modeling with HeFTy (Ketcham, 2005) and QTQt (Gallagher, 2012), PECUBE considers a geothermal gradient and its temporal changes due to heat advection and thermal relaxation in three dimensions (cf. Eizenhöfer et al., 2023; Wolff et al., 2020). Furthermore,

PECUBE allows inverse modeling for a set of samples taken along an elevation profile, that is, it considers the spatial position of the samples relative to each other. A summary and comparison of the capabilities of the different codes mentioned above can be found in van der Beek & Schildgen (2023).

Our modeling approach involved three steps. First, we pre-examined the potential parameter space with respect to exhumation phases and rates by forward modeling with PECUBE. In addition, we also used thermal modeling with HeFTy to obtain constraints on the cooling history of four representative samples (see Text S1 in Supporting Information S1) (cf. Eizenhöfer et al., 2023). In a second step, we performed inverse thermokinematic modeling with PECUBE. The model domain is  $12 \times 12$  km wide, which ensures that cooling ages for the entire set of samples from each profile can be predicted. The model surface represents the present-day topography based on a DEM, which we resampled from a resolution of 10–200 m for the inverse models for computational feasibility. At the base of the 70 km thick model, a temperature boundary condition (800°C) is applied. Note that the model domain does not represent a crust or lithosphere of a certain thickness; the model thickness is only defined to apply a temperature boundary condition and to establish an initial geothermal gradient. Each model is run with the following parameters and boundary conditions: a lapse rate of 6.5°C/km, a surface temperature of 2–10°C, a radiogenic heat production of  $4.0 \times 10^{-6} \text{ W/m}^3$  at the surface, which decreases with depth with an e-folding length of 20 km, a basal temperature of 800°C at 70 km depth, and a thermal diffusivity of  $1.0 \times 10^{-6} \text{ m}^2/\text{s}$  (Stüwe, 2007) (Table 6). These values lead to an initial geothermal gradient of 30°C/km in the upper part of the model (i.e., from the model surface to a depth of  $\sim 5$  km) (Figure S2 in Supporting Information S1). Once exhumation starts, the advection of hot rocks toward the surface causes the geothermal gradient to increase; thermal relaxation decreases the geothermal gradient.

Based on the modeled exhumation history, PECUBE calculates apparent ages for different thermochronometers for samples that have reached the model surface. For computation of these ages, we selected the He diffusion model for apatite of Farley (2000). The diffusion of helium in zircon depends among other parameters mostly on the density of radiation damage (Guenthner, 2021; Guenthner et al., 2013; Whipp et al., 2022). To account for the rather low radiation-damage of our zircon samples with an average of  $5.2 \times 10^{16}$  alpha/g, we adjusted the He diffusion parameters in our model toward lower closure temperature than previously suggested by Reiners et al. (2004). Therefore, we use a value for  $D_0/a^2$  of 37,800 1/s and an activation energy  $E_a$  of 164.1 kJ/mol, which results in a closure temperature of 160°C for a cooling rate of 10°C/Ma (e.g., Whipp et al., 2022). For apatite and zircon fission track we chose the annealing models of Ketcham (2005) and Galbraith and Laslett (1993) with the annealing parameters from Tagami et al. (1998). The misfit  $\phi$  between the cooling ages predicted by the model and the observed ages was calculated as:

$$\phi = \sum_{i=1}^N \left( \frac{\alpha_{i,\text{model}} - \alpha_{i,\text{data}}}{\sigma_{i,\text{data}}} \right)^2$$

where  $N$  is the number of data points,  $\alpha_{i,\text{data}}$  are the observed data,  $\alpha_{i,\text{model}}$  are the predicted values, and  $\sigma_{i,\text{data}}$  is the uncertainty of the ages (Braun et al., 2012). We used an inverse-modeling approach to minimize the misfit between predicted and observed age data of the two elevation profiles. To ensure an efficient exploration of the parameter space we used a two-step neighborhood algorithm inversion (Sambridge, 1999a). For each profile, we performed a total of 16,400 model runs (i.e., 41 iterations with 400 models for each iteration) with a resampling ratio of 0.99. All model calculations were carried out on the high-performance cluster Palma-II of the University Münster. To derive quantitative constraints for the individual parameters and their uncertainties, we use marginal probability density functions (Sambridge, 1999b).

In the third and last step, we performed a forward run with the parameters of the best-fit model. In this forward model, we used the DEM with 10 m resolution to obtain an adequate localization of the closely spaced samples from the two elevation profiles for which we compare modeled and measured cooling ages.

### 3.3.1. Model Assumptions and Limitations

Our inverse PECUBE models are based on the assumptions that the samples move vertically through the model at different rates during the different exhumation phases and that the relative position of the samples to each other does not change during exhumation. Such an exhumation path seems justified because the two areas, in which our samples are located (Figure 3) were primarily exhumed by erosion and not by tectonic denudation. Furthermore, we use the present-day topography, that is, the topography does not change during a model run. The thermal parameters in our models (thermal diffusivity, radiogenic heat production, basal temperature) are laterally constant, whereas in nature, they may vary in space (e.g., Vosteen et al., 2003). Our chosen parameters lead to an initial geothermal gradient of 30°C/km in the uppermost 5 km of the model, which we regard as appropriate for continental crust (e.g., Emmermann & Lauterjung, 1997; Vosteen et al., 2003). Below depths of  $\geq 5$  km, the geothermal gradient decreases continuously. During the model runs, the geothermal gradient may increase owing to heat advection during periods of rapid exhumation and decrease during subsequent thermal relaxation.

## 4. Results From Low-Temperature Thermochronology

The obtained ZFT, ZHe, ZFT, and AHe ages are shown in Figure 4 and reported in Tables 2–5, respectively. In the northeastern Nock Mountains, four samples (19NO29–32) yielded ZFT ages between  $\sim 92$  and  $\sim 84$  Ma and AFT ages between  $\sim 33$  and  $\sim 28$  Ma. In addition, two ZHe ages were obtained from samples 19NO31 ( $78.4 \pm 2.9$  Ma) and 19NO32 ( $82.5 \pm 0.5$  Ma). In the central Nock Mountains, the samples along the elevation profile Innerkrems (Figure 4b; 19NO23–28) yielded ZFT, ZHe and AFT ages of  $\sim 90$ – $83$ ,  $\sim 75$ – $60$ , and  $\sim 33$ – $29$  Ma, respectively. Samples 19NO27 and 19NO28 additionally yielded AHe ages of  $25.1 \pm 4.3$  and  $27.3 \pm 3.8$  Ma, respectively. In the vicinity of the elevation profile, ZFT, ZHe, AFT, and AHe ages of  $93.4 \pm 12.9$ ,  $85.6 \pm 2.9$ ,  $33.4 \pm 4.5$ , and  $31.1 \pm 3.0$  Ma were obtained from sample 14NO13 and AFT and AHe ages of  $36.8 \pm 5.8$  and  $25.1 \pm 1.5$  Ma from sample 14NO1. Three samples (14NO2, 14NO7, 14NO9) located between Innerkrems and the Hochstuhl Fault have AFT ages between  $\sim 36$  and  $\sim 33$  Ma (Figure 4a). South of the Hochstuhl Fault, the samples of the elevation profile Millstatt (Figure 4c) yielded ZFT and AFT ages of  $\sim 47$ – $37$  and  $\sim 19$ – $14$  Ma, respectively. In addition, a ZHe age of  $23.1 \pm 1.4$  Ma was obtained from sample 19NO19 and an AHe age of  $12.7 \pm 2.2$  from sample 19NO21. Sample (19NO33) in the southeastern part of the study area yielded ZFT, ZHe, and AFT ages of  $90.9 \pm 7.7$ ,  $73.5 \pm 4.4$ , and  $28.6 \pm 5.0$  Ma (Figure 4a).

## 5. Results From Thermokinematic Modeling

The cooling ages of samples, to which 2 or more thermochronometers could be applied (e.g., 14NO13, 19NO32, 19NO33), indicate that the Gurktal Alps did not cool at a constant rate (Tables 2–5, Figure 4). Also, the large difference between the clusters of ZFT and AFT ages obtained from the two elevation profiles at Innerkrems and Millstatt as well as the narrow range of  $<10$  Ma for both the ZFT and AFT ages along each profile cannot be explained by a single phase of cooling and exhumation (Figure 4). This is also supported by thermal modeling with the software HeFTy (Figure S1 in Supporting Information S1). For thermokinematic modeling with PECUBE, we therefore allowed the exhumation rate to change twice in each model run, that is, our approach employs an exhumation history consisting of three phases, with each phase having a different but temporally constant exhumation rate. As a consequence, each inverse model has a total of six free parameters, which are considered simultaneously in each model computation. The six parameters are the exhumation rate and the onset of exhumation for each of the three exhumation phases.

For the Innerkrems profile (Figure 5), where ZFT ages cluster around 90 Ma, the first exhumation phase was allowed to begin between 105 and 90 Ma with an exhumation rate ranging from 0.4 to 0.8 km/Ma. The time when the exhumation rate drops to a lower value (i.e., the beginning of Phase 2) was varied between 90 and 50 Ma, with the exhumation rate during Phase 2 ranging from 0.01 to 0.06 km/Ma. The final exhumation Phase 3 starts between 50 and 0 Ma with an exhumation rate between 0.14 and 0.18 km/Ma. The results of the inversion procedure are shown in Figure 5, in which the best-fit model is indicated by a star. Taken together, the best-fit model indicates that exhumation started at  $99.3 \pm 3.4$  Ma at a rate of  $0.60 \pm 0.06$  km/Ma. At  $82.5 \pm 3.1$  Ma, exhumation

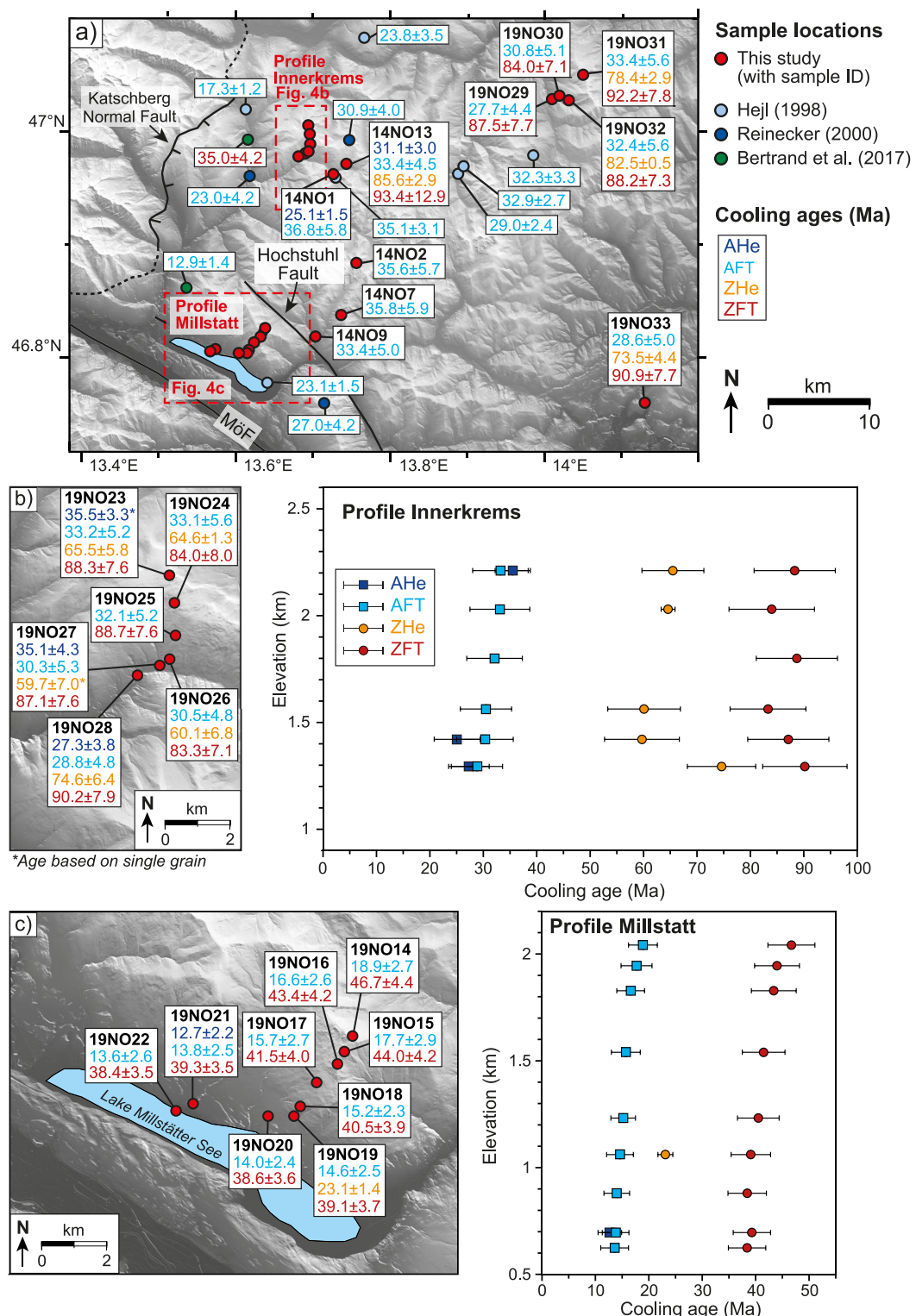


**Figure 4.** Shaded relief images with thermochronological data from this and earlier studies. (a) Overview map. (b) Innerkrembs elevation profile and (c) Millstatt elevation profile.

slowed down to a rate of  $0.02 \pm 0.01$  km/Ma. During the third exhumation phase ( $33.8 \pm 1.8$  Ma to present), exhumation proceeded at a rate of  $0.16 \pm 0.02$  km/Ma. Cooling ages predicted by the best-fit model and the measured age data are shown in Figure 5b. The modeled and observed ZFT and AFT ages are in good agreement,

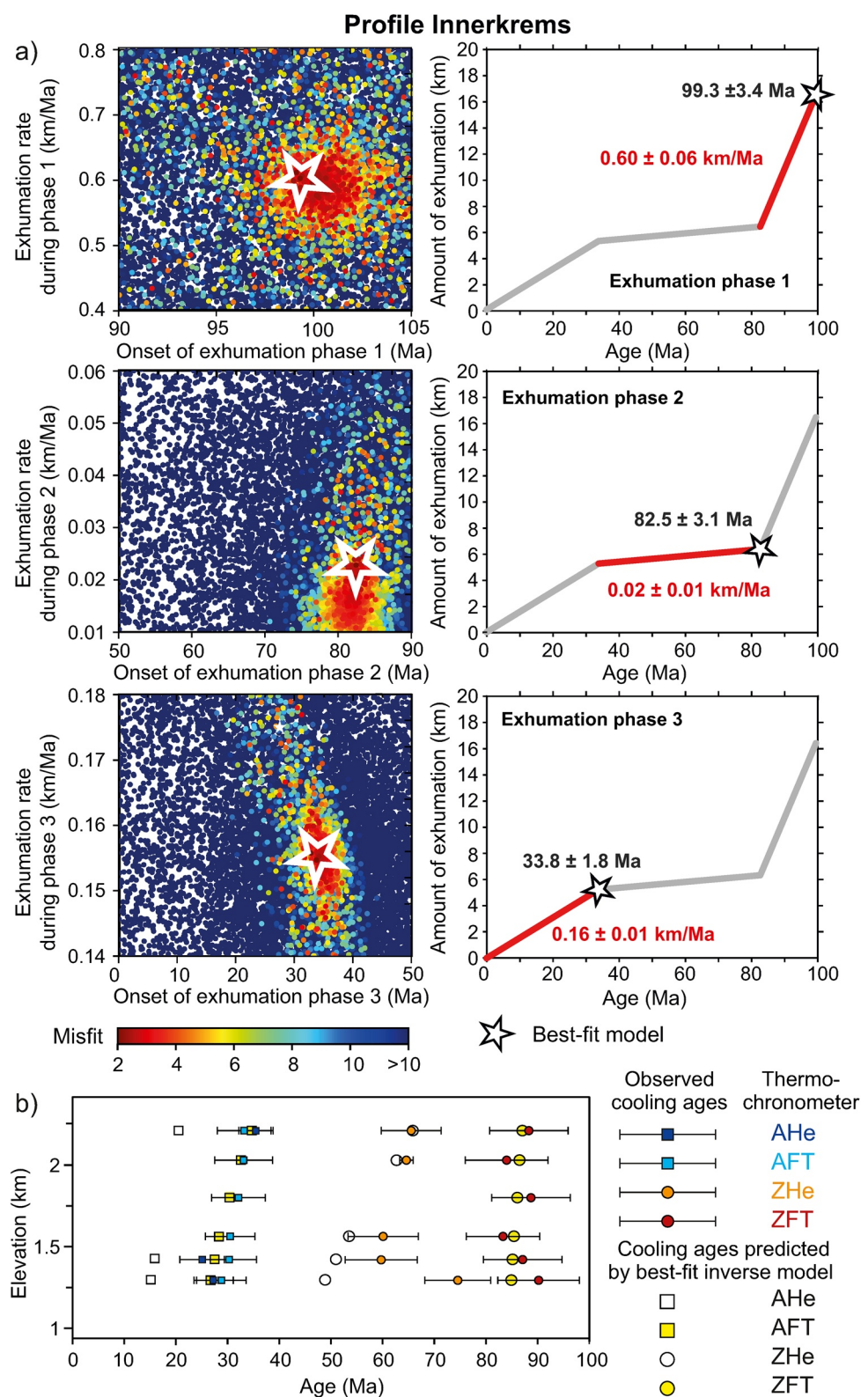


Figure 5.

whereas modeled and measured ZHe ages agree for higher elevations but deviate at lower elevation. Modeled AHe ages are consistently younger than the observed AHe ages.

In the inverse model used for the Millstatt profile (Figure 6), the onset of exhumation Phase 1 and the respective exhumation rate were allowed to vary between 48 and 40 Ma and between 0.5 and 1.0 km/Ma, respectively. The time when the exhumation rate drops to a lower value (i.e., the beginning of Phase 2) was allowed to vary between 40 and 30 Ma, while the exhumation rate during Phase 2 ranges from 0.05 to 0.2 km/Ma. The final exhumation Phase 3 starts between 30 and 0 Ma with an exhumation rate ranging from 0.1 to 0.5 km/Ma. In the best-fit model, exhumation begins at  $43.7 \pm 2.3$  Ma and proceeds at a rate of  $0.76 \pm 0.05$  km/Ma until  $38.5 \pm 1.8$  Ma, when exhumation slows down to a rate of  $0.13 \pm 0.03$  km/Ma. Exhumation Phase 3 starts at  $18.3 \pm 2.2$  Ma at a rate of  $0.27 \pm 0.03$  km/Ma and continues until the present. The ages predicted by the best-fit model and the measured age data are shown in Figure 7b. All modeled and observed ZFT and AFT ages as well as the single ZHe age are in very good agreement. Notably, the model also captures the non-linear increase of AFT and ZFT ages with elevation. Similar to the Innerkrems profile, the modeled AHe age is younger than the measured age.

Under the assumption that rock uplift is balanced by erosion and that the topography did not change, the results of the inverse modeling allow estimating the thickness of the rock pile, which has been removed during exhumation of the Innerkrems and Millstatt areas. The amount of overburden removed during each exhumation phase is calculated from the best-fit model using the duration of the three different phases and their respective exhumation rates. For the Innerkrems profile, the modeled exhumation history starts at  $\sim 100$  Ma and involved the removal of  $\sim 16$  km of rocks (Figure 5a). For the Millstatt profile, the best-fit model indicates that exhumation began at  $\sim 44$  Ma and that  $\sim 11$  km of rock were removed during the entire exhumation history (Figure 6a).

## 6. Discussion

Our thermochronological data set reveals distinct differences in the cooling ages obtained from the Austroalpine units in the northeastern and central Nock Mountains (Ötztal-Bundschnuh and Drauzug-Gurktal nappes) compared to the units exposed south of the Hochstuhl Fault (Radenthein and Millstatt Complexes) (Figures 3 and 4). In particular, the Late Cretaceous cooling history is constrained by ZFT ages from the northeastern and central Nock Mountains, whereas the same thermochronometer yields Eocene cooling ages in the southern Nock Mountains. For both regions, thermokinematic modeling of the two elevation profiles (Innerkrems and Millstatt) revealed alternating phases of enhanced and slow exhumation of the Austroalpine units in the Gurktal Alps. The timing of these phases differs considerably north and south of the Hochstuhl Fault, suggesting that phases of rapid exhumation were caused by different tectonic events. In the following, we discuss our results in the light of the tectonic evolution of the Eastern Alps.

### 6.1. Exhumation History of Austroalpine Units Located at a High Structural Level and North of the Indenter (Central and Northeastern Nock Mountains)

Austroalpine units of the northeastern and central Nock Mountains (Drauzug-Gurktal and Ötztal-Bundschnuh nappes) consistently show ZFT ages between  $\sim 93$  and  $\sim 83$  Ma (Figures 4 and 5; Table 2). ZHe ages are younger in the Ötztal-Bundschnuh nappe (75–60 Ma) than in the Drauzug-Gurktal nappe (86–78 Ma). Based on the best-fit PECUBE model of the Innerkrems profile, the exhumation rate between  $99.3 \pm 3.4$  and  $82.5 \pm 3.1$  Ma is  $0.60 \pm 0.06$  km/Ma (Figures 5 and 7). We consider this exhumation phase to reflect cooling after formation of the Austroalpine nappe stack (Kurz & Fritz, 2003; Ratschbacher & Neubauer, 1989) and the Eo-Alpine metamorphism, which reached peak pressure conditions at  $\sim 100$ –90 Ma (Miladinova et al., 2022; Neubauer et al., 2003; Schuster & Frank, 1999). This Late Cretaceous phase of exhumation was presumably related to top-to-the-ESE extension that occurred while WNW-directed thrusting was still active at deeper crustal levels (Figure 8a) (Faupl & Wagreich, 2000; Kurz & Fritz, 2003; Mandl, 2000; Ratschbacher et al., 1989). In the Gurktal Alps, Late Cretaceous extension is documented by petrological and structural data, which show that Eo-Alpine thrust faults were

**Figure 5.** Results from thermokinematic inverse modeling with six free parameters for the Innerkrems elevation profile. (a) Left column: Diagrams showing the parameter space defined by the exhumation rate and the onset of exhumation for each of the three exhumation phases. Each dot represents the parameter combination in one of the inverse models with the color of the dot representing the model misfit. The star in each diagram marks the parameter combination extracted from the best-fit model. Note that the inverse modeling solves for all six free parameters simultaneously, that is, each model covers the entire three-phase exhumation history. To be able to depict the inversion results obtained in the 6D parameter space, we show them for each exhumation phase in separate diagrams as 2D parameter space. Right column: Depth-versus-age diagrams showing the onset of each exhumation phase and the respective exhumation rate during each phase as obtained from the best-fit model. (b) Age-elevation diagrams showing the measured cooling ages in comparison to the cooling ages obtained from the best-fit model.

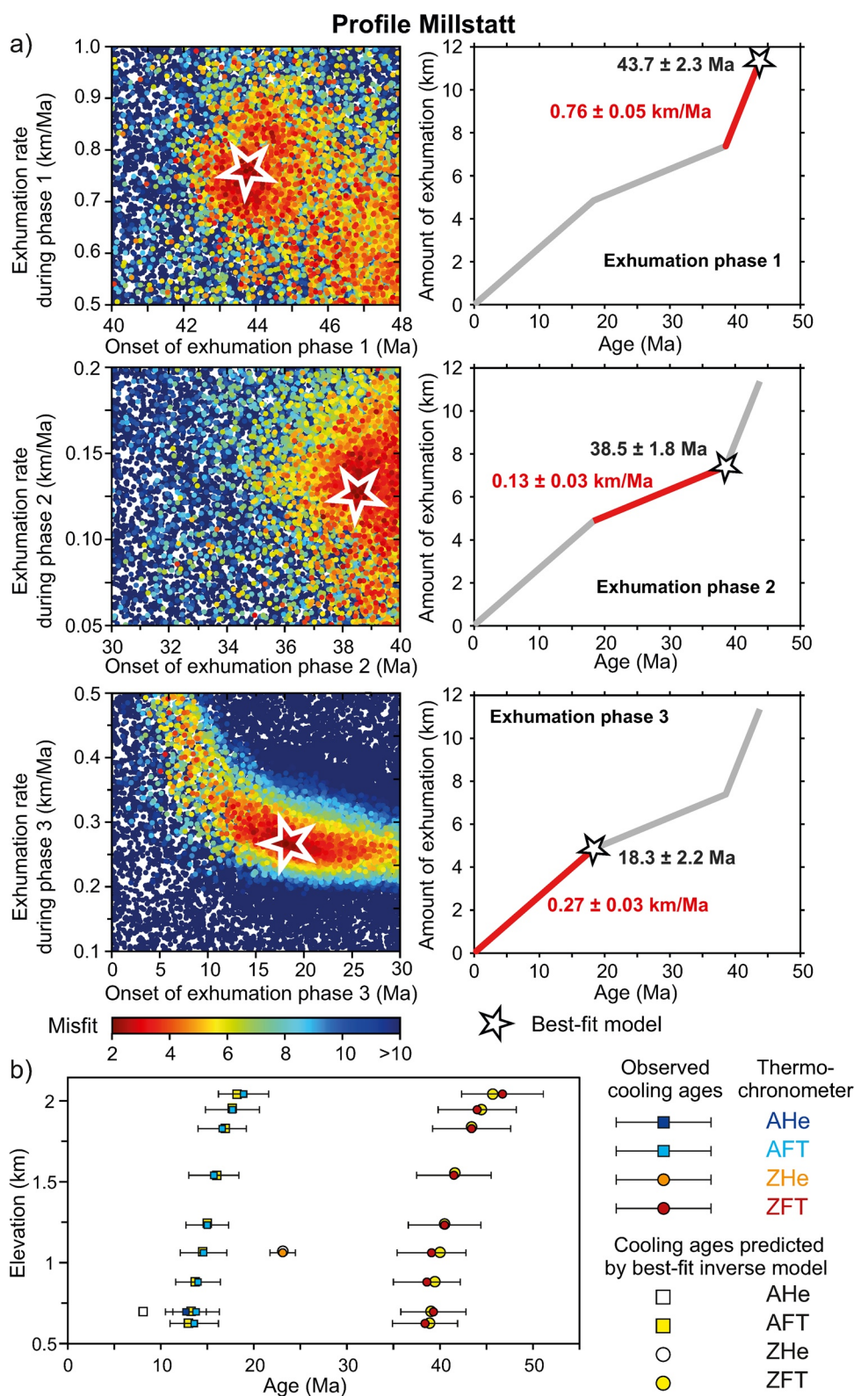
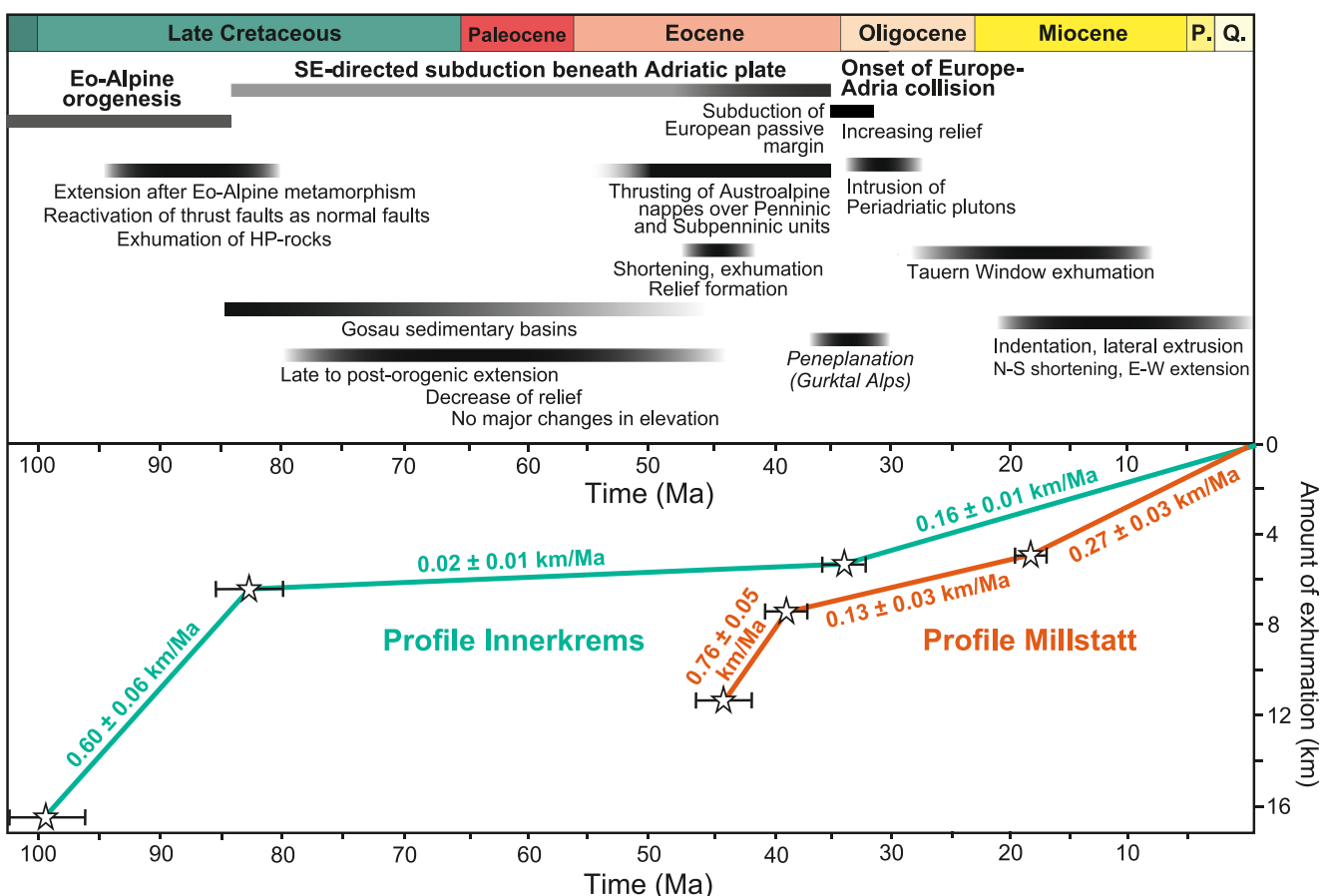


Figure 6.



**Figure 7.** Overview of major events during the evolution of the Eastern Alps and comparison with modeled best-fit exhumation phases of the Innerkrems and Millstatt elevation profiles. The events and their timing have been compiled from the following studies: Tollmann (1986), Frank et al. (1987), Ratschbacher et al. (1989), Ratschbacher, Merle, et al. (1991), Ratschbacher, Frisch, et al. (1991), Wagreich and Faupl (1994), von Blanckenburg & Davies (1995), Oberhauser (1995), Schmid et al. (1996), Sissling (1997), Frisch et al. (1998), Hoinkes et al. (1999), Koroknai et al. (1999), Frisch, Dunkl, and Kuhlemann (2000), Frisch, Székely, et al. (2000), Liu et al. (2001), Wagreich (2001), Linzer et al. (2002), Kázmér et al. (2003), Dunkl et al. (2005), Thöni (2006), and Handy et al. (2010, 2015).

reactivated as normal faults (Figure 8a) (Koroknai et al., 1999; Rantitsch et al., 2020). Top-to-the-ESE normal faulting may explain the difference in ZHe ages obtained from the central and northeastern Nock Mountains (Figure 4), because it placed the Drauzug-Gurktal nappe in a hanging-wall position relative to the Ötztal-Bundschuh nappe in the footwall (Figures 3c and 8) (Koroknai et al., 1999; Rantitsch et al., 2020). Late Cretaceous extension was, however, not limited to the Gurktal Alps but occurred orogen-wide, as indicated by normal faulting in the entire Austroalpine nappe stack (e.g., Schuster et al., 2013), including Austroalpine units exposed in the Saualpe, Koralpe and other regions east of the Gurktal Alps (Krenn et al., 2008; Krohe, 1987; Kurz et al., 2002; Neubauer et al., 1995; Rantitsch et al., 2005; Schorn & Stüwe, 2016; Wiesinger et al., 2006), in the Kreuzeck block southeast of the Tauern window (Griesmeier et al., 2018; Hoke, 1990; Wölfler, Frisch, et al., 2015) and in the Ötztal Alps west of the Tauern Window (Froitzheim et al., 1997; Fügenschuh et al., 2000; Krenn et al., 2011; Ratschbacher et al., 1989). Extensional deformation resulted in rapid cooling of high-pressure rocks below  $\sim 400^\circ\text{C}$  until ca. 85 Ma (Thöni, 2006; Wiesinger et al., 2006) and in the formation of the Gosau sedimentary basins, which started in the Late Santonian at  $\sim 86$  Ma with coarse-grained alluvial deposits (Willingshofer et al., 1999) (Figure 8a).

**Figure 6.** Results from thermokinematic inverse modeling with six free parameters for the Millstatt elevation profile. (a) Left column: Diagrams showing the parameter space defined by the exhumation rate and the onset of exhumation for each of the three exhumation phases. Each dot represents the parameter combination in one of the inverse models with the color of the dot representing the model misfit. The star in each diagram marks the parameter combination extracted from the best-fit model. Note that the inverse modeling solves for all six free parameters simultaneously, that is, each model covers the entire three-phase exhumation history. To be able to depict the inversion results obtained in the 6D parameter space, we show them for each exhumation phase in separate diagrams as 2D parameter space. Right column: Depth-versus-age diagrams showing the onset of each exhumation phase and the respective exhumation rate during each phase as obtained from the best-fit model. (b) Age-elevation diagrams showing the measured cooling ages in comparison to the cooling ages obtained from the best-fit model.

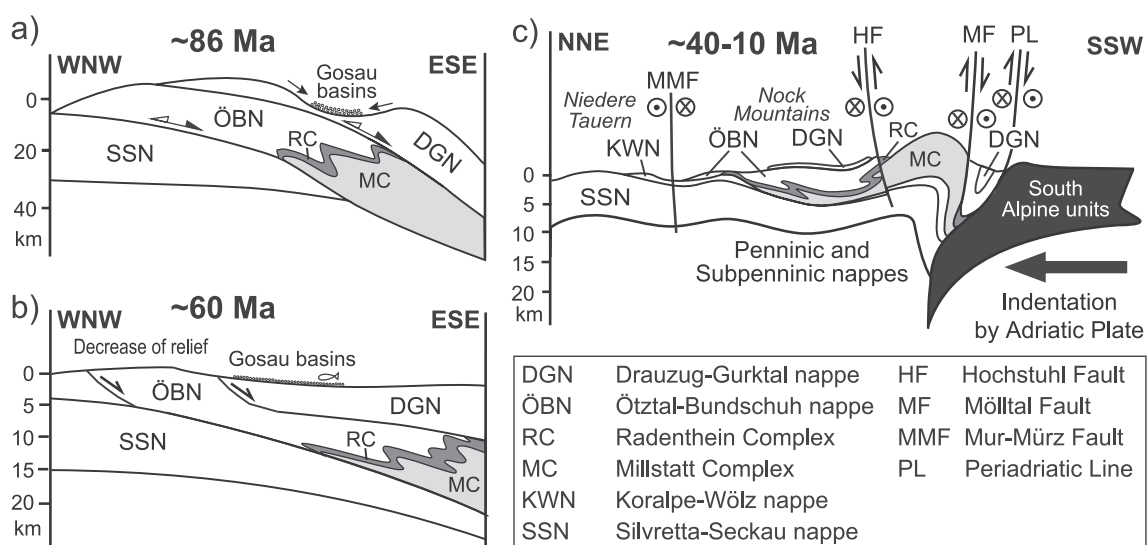


**Figure 8.** Schematic cross-sections (not to scale) of the configuration and structural position of the Austroalpine nappes in the Gurktal Alps based on Krenn et al. (2011) taking into account the results from this study and the findings by Klug and Froitzheim (2022). (a) Late Cretaceous extension and onset of deposition of Gosau sediments. (b) Paleocene. (c) Late Eocene to Late Miocene. Note that strike-slip faulting on Mölltal, Hochstuhl, and Mur-Mürz Faults commenced in the Miocene as a result of lateral extrusion.

Based on our modeling results for the central Nock Mountains, a transition to slower exhumation at a rate of  $0.02 \pm 0.01$  km/Ma occurred at  $\sim 83$  Ma (Figure 5), which may be explained by the end of extensional deformation. The period of slower exhumation lasted until  $\sim 34$  Ma (Figure 5). A prolonged phase of slow exhumation in the northern Gurktal Alps since the Eo-Alpine orogeny is also indicated by fission track age distributions for detrital apatite determined from Miocene sediments in basins in the Eastern Alps (Dunkl et al., 2005). These detrital age distributions indicate that  $\sim 1.5$  km of rocks were removed by erosion before the Miocene (Dunkl et al., 2005), which is consistent with the amount of exhumation obtained from our Innerkrems profile. The phase of slow exhumation coincides with a phase without major changes in elevation in the Paleocene and Early Eocene in the Eastern Alps (Figures 7 and 8) (Dunkl et al., 2005; Kázmér et al., 2003; Oberhauser, 1995; Wagreich & Faupl, 1994), during which shallow marine sediments of Palaeocene and Eocene age (Oberhauser, 1995) were deposited on the metamorphic units of the Austroalpine nappes. The persistence of slow exhumation throughout the Eocene implies that the central Nock Mountains do not show a thermochronological signal of the events that indicate shortening in the Eastern Alps during the Eocene (Figures 7 and 8; see Section 6.2). Our AFT and AHe data (Figure 4) and AFT ages from earlier studies (Hejl, 1997, 1998; Reinecker, 2000) indicate that the central and northeastern Nock mountains resided at an upper crustal level ( $< 5\text{--}6$  km depth) since the Eocene-Oligocene boundary (Figures 5a and 7). At  $33.8 \pm 1.8$  Ma, the exhumation rate increased to  $0.16 \pm 0.02$  km/Ma (Figure 5), which coincides with the onset of the Europe-Adria collision at  $\sim 35$  Ma (Figure 7) (Handy et al., 2010; Rosenberg et al., 2018). During this time, most parts of the Eastern Alps experienced uplift and an increase in elevation, which is reflected by the beginning of coarse-grained clastic sedimentation in the Molasse basin at  $\sim 30$  Ma (Kuhlemann & Kempf, 2002; Kuhlemann et al., 2002, 2008; Lemcke, 1988). In the Gurktal Alps, the relief remained rather low, and widespread peneplanation occurred until  $\sim 30$  Ma (e.g., Dunkl et al., 2005; Frisch, Székely, et al., 2000). Afterward, topography also increased in the Nock Mountains, which, however, did not develop a mountainous relief but were rather characterized by lowlands and a hilly landscape (Frisch et al., 1998). The beginning of our modeled third exhumation phase ( $\sim 34$  Ma) also coincides with an early phase of exhumation of the Penninic units in the future Tauern Window in the Early Oligocene, as indicated by geochronological data (Favaró et al., 2015; Schneider et al., 2015) and detrital thermochronology (Hülscher et al., 2021).

## 6.2. Exhumation History of Austroalpine Units at Lower Structural Levels and Located Close to the Indenter (Southern Nock Mountains)

In contrast to the central and northeastern Nock Mountains, ZFT ages from the southern Nock Mountains are significantly younger (47–37 Ma) and the samples constrain the cooling history since the Middle Eocene (Figure 4).

This implies that the Millstatt and Radenthein Complexes (Figure 3), to which the sampled rocks belong, were at higher temperatures, that is, above the ZFT closure temperature, until the Middle Eocene. This is consistent with their position at a deeper structural level than the units exposed in the central Nock Mountains (Figures 1c and 3c) (Krenn et al., 2011; Schuster et al., 2013) and with petrological studies that documented the peak of amphibolite facies metamorphism at  $\sim$ 90 Ma (Hoinkes et al., 1999; Thöni, 2006). Based on the best-fit model from the Millstatt profile, cooling below the ZFT closure temperature commenced at  $43.7 \pm 2.3$  Ma and continued until  $38.5 \pm 1.8$  Ma at a rate of  $0.76 \pm 0.05$  km/Ma (Figures 5 and 7). It should be noted that this cooling phase may have started before  $\sim$ 44 Ma because the cooling from temperatures higher than the ZFT closure temperature to the ZFT closure temperature is not constrained in our data. Our modeled phase of fast exhumation between  $\sim$ 44 (or earlier) and 38 Ma falls within the time period when the Austroalpine nappes were thrusted over Penninic and Subpenninic units (Figure 7). If our modeled onset of the exhumation phase ( $43.7 \pm 2.3$  Ma) indeed marks the onset of enhanced exhumation, it temporally coincides with the beginning subduction of the distal European passive margin after the Early Eocene (Neubauer et al., 2000), presumably around 45 Ma (Schmid et al., 2013). We therefore interpret our modeled phase of exhumation to be related to an Eocene phase of shortening prior to the continental collision between Europe and Adria (Figure 7) (Dunkl et al., 2005; Faupl & Wagreich, 2000; Handy et al., 2010; Linzer et al., 2002; Tollmann, 1986; Wagreich, 2001). In the eastern Swiss Alps, such a phase of shortening is known as the Blaisun phase (50–35 Ma), during which  $>75$  km of top-N-thrusting of Austroalpine and previously accreted Upper Penninic units over deeper Penninic units occurred and the Austroalpine nappes may have been internally folded (Froitzheim et al., 1994; Pfiffner, 2009). In the Eastern Alps, two  $^{40}\text{Ar}/^{39}\text{Ar}$  muscovite ages of  $\sim$ 51 and  $\sim$ 55 Ma from the lowermost Austroalpine nappe were interpreted to date ductile shearing during thrusting of the Austroalpine units above the Penninic units, because the Alpine metamorphism of this nappe did not exceed 350–400°C (Liu et al., 2001). Shortening, relief formation and erosion in the Eastern Alps during the Eocene is further supported by coarse-grained mass flow deposits in the uppermost part of several of the Gosau basins in the Northern Calcareous Alps include a siliciclastic component (Wagreich, 2001). The sedimentary facies evolution of these sediments and the timing of the end of sedimentation indicates a northward propagation of thrusting during the Paleocene and Eocene (Wagreich, 2001). In some Gosau basins, the sediments are truncated by thrust faults, which provides further evidence for crustal shortening during this time (Faupl & Wagreich, 2000). The observation that garnet dominates the heavy mineral spectrum suggests that the sediments were partly derived from eroding Austroalpine basement complexes located farther to the south (i.e., in the area of the Gurktal Alps) (Wagreich, 2001). That relief formation, erosion and exhumation in the Gurktal Alps largely occurred during the Middle Eocene is indicated by fission track age distributions for detrital apatite from Miocene sediments in basins of the Eastern Alps indicate a phase of increased erosion during the middle Eocene (Dunkl et al., 2005). Assuming a geothermal gradient of 30°C/km, Dunkl et al. (2005) estimated that a minimum of 2 km and a maximum 6 km of erosion occurred in the southern and central parts of the Eastern Alps. The range of 2–6 km of erosion is consistent with the amount of  $\sim$ 4 km of exhumation obtained from the Millstatt profile (Figure 7). In addition, our thermokinematic modeling provides constraints on the exhumation rate ( $0.76 \pm 0.05$  km/Ma) for the onset ( $43.7 \pm 2.8$  Ma or earlier) and end ( $38.5 \pm 1.8$  Ma) of this Eocene exhumation phase. Enhanced exhumation during the Eocene has also been documented for the Polinik block south of the Tauern Window (Figure 2, Wölfler et al., 2008; Wölfler, Frisch, et al., 2015). As the Polinik block occupies a low structural level (Koralpe-Wölz nappe) in the Austroalpine nappe stack, its exhumation may be related to Eocene shortening prior to the Europe-Adria collision, similar to the exhumation of the southern Nock Mountains.

As indicated by our Millstatt model, the Middle Eocene phase of fast exhumation was followed by a period of slower exhumation ( $0.013 \pm 0.03$  km/Ma) in the Late Eocene and Early Oligocene (Figure 7). This implies that rocks south of the Hochstuhl Fault do not show a thermochronological signal of the onset of the Europe-Adria collision at  $\sim$ 35 Ma (Handy et al., 2010), in contrast to the structurally higher units in the central and northeastern Nock Mountains. Only after  $\sim$ 18 Ma, the exhumation rate increased again to  $0.27 \pm 0.03$  km/Ma, which we interpret as a result of the indentation of the Eastern Alps by the Adriatic Plate and the lateral extrusion in the Miocene (Caporali et al., 2009; Frisch, Dunkl, & Kuhlemann, 2000; Ratschbacher, Frisch, et al., 1991; Ratschbacher, Merle, et al., 1991; Rosenberg, 2004; Rosenberg et al., 2004, 2007; Scharf et al., 2013; Wölfler et al., 2011). Thermochronological data indicating faster exhumation in the course of Miocene indentation and lateral extrusion have also been reported from Austroalpine nappes south of the Tauern Window (e.g., Luth & Willingshofer, 2008; Steenken et al., 2002; Stöckhert et al., 1999; Wölfler et al., 2008; Wölfler, Dekant, et al., 2015; Wölfler, Frisch, et al., 2015), in the Niedere Tauern (Wölfler et al., 2016) and east of the Gurktal Alps (van Gelder et al., 2020). In particular, the Austroalpine units between the southern border of the Tauern Window and the Periadriatic Line,

that is, in front of the Adriatic indenter, were fragmented into rigid, wedge-shaped blocks (Figure 1) and experienced substantial exhumation by erosion during the Miocene, contemporaneous with the Penninic units of the Tauern Window (Luth & Willingshofer, 2008; Rosenberg et al., 2018; Scharf et al., 2013; Steenken et al., 2002; Stöckhert et al., 1999; Wölfler et al., 2008; Wölfler, Dekant, et al., 2015; Wölfler, Frisch, et al., 2015). Coeval with enhanced exhumation of the southern Nock Mountains, sedimentation in pull-apart basins along the SEMP and the MMF as well as in the Styrian basin started at ~18 Ma (Figure 1) (e.g., Fodor et al., 1999; Sachsenhofer et al., 1997, 2000). Since basin formation in the Eastern Alps has been interpreted in terms of tectonic escape toward the east (Frisch, Dunkl, & Kuhlemann, 2000; Linzer et al., 2002; Ratschbacher, Frisch, et al., 1991; Ratschbacher, Merle, et al., 1991; Wölfler et al., 2011), both, northward indentation by the Adriatic plate as well as E-W extension contributed to shaping the Eastern Alps since the Miocene (e.g., Ratschbacher et al., 1989; Ratschbacher, Frisch, et al., 1991; Ratschbacher, Merle, et al., 1991; Rosenberg et al., 2018). Our results from the Gurktal Alps are consistent with the notion that indentation-induced thrust faulting and rock exhumation by erosion dominated in front of the indenter, that is, in the southern part of the Eastern Alps, whereas most of the area east of the Tauern Window experienced predominantly strike-slip faulting as a result of tectonic escape as well as E-W extension (Figures 1 and 8) (e.g., Frisch, Dunkl, & Kuhlemann, 2000; Ratschbacher, Frisch, et al., 1991; Ratschbacher, Merle, et al., 1991; Rosenberg et al., 2018; Scharf et al., 2013; Wölfler et al., 2011).

### 6.3. Implications for the Evolution of the Austroalpine Nappes

Our data and thermokinematic models show that the structurally higher Drauzug-Gurktal and Ötztal-Bundschuh nappes in the central and northeastern Nock Mountains have a different cooling and exhumation history compared to the structurally lower Radenthein and Millstatt Complexes located south of the Hochstuhl Fault (Figures 1, 3, and 4). While the Radenthein and Millstatt Complexes (Figure 3) experienced enhanced exhumation related to an Eocene phase of shortening prior to the Europe-Adria collision and during Miocene N-S shortening, crustal thickening, erosion and lateral extrusion, these events are not reflected in the cooling history of the structurally higher units in the central and northeastern Nock Mountains (Figure 7). On the other hand, the Europe-Adria collision is recorded by the beginning of enhanced exhumation at the Eocene-Oligocene boundary in the central and northeastern Nock Mountains but it did not leave a signal in the cooling history of the Radenthein and Millstatt Complexes (Figure 7). The difference in the cooling history may be explained by different position of the respective units in the Austroalpine nappe stack and relative to the Adriatic indenter (Figures 1b and 1c).

Altogether, ~16 km of rock were removed since ~99 Ma in the Innenkrems region, whereas ~11 km of rock were removed in the last ~44 Ma in the Millstatt area (Figures 5–7). This is consistent with the pressure-temperature estimates for the metamorphic conditions experienced by the Ötztal-Bundschuh nappe and Radenthein/Millstatt Complexes, respectively (Figure 3c) (Koroknai et al., 1999; Krenn et al., 2011; Schuster, 2003). Based on these findings, we argue that the Drauzug-Gurktal and Ötztal-Bundschuh nappes of the central and northeastern Nock Mountains are kinematically separated from the Radenthein and Millstatt Complexes by the Hochstuhl Fault since at least the Middle Eocene (Figures 3, 7, and 8). A comparison between the thermokinematic models for the Millstatt and Innenkrems profiles (Figure 7) shows that between ~44 and ~39 Ma the Radenthein and Millstatt Complexes were exhumed by ~4 km (i.e., from ~12 to ~8 km depth) relative to Ötztal-Bundschuh nappe, which resided at a depth of ~5 km during this period. Notably, the grade of Eo-Alpine metamorphism increases more or less continuously southward in the Ötztal-Bundschuh nappe, whereas the boundary between the Ötztal-Bundschuh nappe and the Radenthein Complex is offset by the Hochstuhl fault (Figure 3c) (Schuster et al., 2013). The absence of this boundary south of the Hochstuhl fault indicates that the Radenthein Complex was uplifted relative to the Ötztal-Bundschuh nappe north of the Hochstuhl fault. Based on the difference in the amount of exhumation of ~4 km revealed by our thermokinematic models (Figure 7) and the offset indicated in the cross-section of Schuster et al. (2013) (Figure 3c), we argue that the Hochstuhl fault may have accommodated some vertical movement between ~44 Ma (or earlier, see above) and ~39 Ma. Given that this time period overlaps with the phase of mid-Eocene shortening (see Section 6.2, Dunkl et al., 2005; Froitzheim et al., 1994; Wagreich, 2001), we suggest that the Hochstuhl fault was active as a steep, SSW-dipping reverse fault (Figure 8c). During faulting, the southern block occupied a hanging-wall position and was exhumed by erosion, whereas the Drauzug-Gurktal and Ötztal-Bundschuh nappes farther north in the central and northeastern Nock Mountains continued to be slowly exhumed until ~34 Ma (Figures 4 and 7). Note that our interpretation of some thrust movement on the Hochstuhl fault between ~44 (or earlier) and ~39 Ma does not exclude that contractional deformation during the Eocene may also have been accommodated by some folding within Radenthein and Millstatt

Complexes. Such folding would also have caused uplift relative to the central Nock Mountains, erosion and exhumation (Figure 8c) (cf. Bertrand et al., 2017; Rosenberg et al., 2015, 2018).

Since  $\sim 34$  Ma, only  $\sim 5$  km of rock have been removed in the central Nock Mountains. In contrast, the eastern Tauern Window in the footwall of the Katschberg normal fault experienced the removal of more than 25 km of rock since  $\sim 23$  Ma by a combination of normal faulting and erosion (Favarro et al., 2017; Scharf et al., 2013). This profound difference may be explained by the fact that the central and northeastern Nock Mountains are located in the hanging wall of the Katschberg normal fault and bounded by strike-slip faults to the north (MMF) and south (Hochstuhl Fault) (Figure 1). As a consequence, the Drauzug-Gurktal and Ötztal-Bundschuh nappes in the central and northeastern Nock Mountains were slowly exhumed by erosion and remained largely unaffected by exhumation in the wake of Miocene indentation and E-W extension. In contrast, the crustal block between the Hochstuhl and Mölltal Faults, which is located in front of the indenter, experienced  $\sim 7$ – $8$  km of rock removal since  $\sim 39$  Ma, of which  $\sim 5$  km were removed after  $\sim 18$  Ma (Figure 7). The difference in the amount of exhumation north and south of the Hochstuhl fault may have resulted from folding (Krenn et al., 2011) and/or some minor vertical movement on the Hochstuhl fault (Figure 8c). The latter may be indicated by the marked difference in AFT ages across the Hochstuhl fault (Figures 4a and 4c).

With respect to the two orogenic phases in the Eastern European Alps, our data and thermokinematic models show that the Ötztal-Bundschuh and Drauzug-Gurktal nappes east of the Tauern Window have preserved the exhumation record of syn- to late-orogenic extension in the course of the Cretaceous orogeny (Schmid et al., 2008; Schuster, 2003; Schuster et al., 2013), the long phase of relative tectonic quiescence without major changes in elevation from the Late Cretaceous to the Middle Eocene (Dunkl et al., 2005; Oberhauser, 1995; Wagreich & Faupl, 1994) and finally the Paleogene orogeny (Schmid et al., 1996), Miocene N-S shortening including crustal thickening and erosion (Rosenberg et al., 2015, 2018) and lateral extrusion (Frisch, Dunkl, & Kuhlemann, 2000; Ratschbacher, Frisch, et al., 1991; Ratschbacher, Merle, et al., 1991). A similar preservation of the exhumation history since the Cretaceous may be expected for the equivalent part of the Ötztal-Bundschuh nappe that is located west of the Tauern Window in the Ötztal Alps where ZFT ages range between 99 and 71 Ma (Figures 1 and 2) (Elias, 1998; Fügenschuh et al., 1997, 2000). However, no age-elevation profiles or thermokinematic models are available so far for the Ötztal Alps. In contrast, the crustal blocks between the Tauern Window and the Periadriatic Line may show distinct differences in cooling histories, as illustrated by the ZFT cooling ages from the Polinik and Kreuzeck blocks (Figure 2) (Dunkl et al., 2003; Wölfler et al., 2008; Wölfler, Dekant, et al., 2015). Similar to the Ötztal-Bundschuh and Drauzug-Gurktal nappes in the central Nock Mountains, the Kreuzeck block (Figure 2) has recorded Late-Cretaceous extension, whereas the Polinik block (Figure 2) shows Eocene to Oligocene ZFT ages similar to the Radenthein and Millstatt Complexes in our study area. As in the Gurktal Alps, the differences in cooling histories may be related to the different position of the Kreuzeck and Polinik blocks within the Austroalpine nappe stack and relative to the Adriatic indenter (Wölfler et al., 2008).

## 7. Conclusions

New low-temperature thermochronological ages and thermokinematic modeling of two elevation profiles allowed us to constrain the exhumation history of the Austroalpine units in the Gurktal Alps east of the Tauern Window. Our results reveal that the Austroalpine units experienced two phases of enhanced exhumation separated by a period of slow cooling, but that these phases occurred at different times and are related to different tectonic events. Whereas ZFT ages from the structurally higher units (Ötztal-Bundschuh and Drauzug-Gurktal nappes; central and northeastern Nock Mountains) document enhanced cooling driven by late-orogenic extension in the Late Cretaceous, ZFT ages from structurally lower Radenthein and Millstatt Complexes (southern Nock Mountains) indicate enhanced cooling between  $\sim 44$  (or earlier) and  $\sim 39$  Ma. Our modeled timing of enhanced Eocene exhumation temporally correlates with a phase of shortening and relief formation in the Eastern Alps, which ended the sedimentation in the Gosau Basins (e.g., Dunkl et al., 2005; Faupl & Wagreich, 2000; Wagreich, 2001) and occurred during the thrusting of Austroalpine units over Penninic and Subpenninic units (e.g., Liu et al., 2001; Neubauer et al., 2000; Schmid et al., 2013). Our study provides the first quantitative constraints on the timing and rate of exhumation of the Austroalpine nappes during this Eocene phase of shortening, which preceded the Europe-Adria collision and may correlate with the Blaibach phase of N-S shortening in the eastern Swiss Alps (Froitzheim et al., 1994; Pfiffner, 2009). The second phase of faster exhumation started with the onset of the Europe-Adria collision for the structurally higher units in the central Nock Mountains, whereas for the structural lower units in the southern Nock Mountains, it began with Miocene N-S shortening and lateral extrusion.

More generally, our study highlights that the exhumation histories of the Austroalpine nappes are strongly controlled by their structural position within the nappe stack and their distance to the northern margin of the Adriatic indenter. Nappes at high structural levels and farther away from the indenter (e.g., Ötztal-Bundschuh nappe) represent a unique geological archive from which the exhumation history during and after the Eo-Alpine orogeny can be reconstructed (i.e., the period after ~100 Ma with late-orogenic extension and the subsequent phase without major deformation until the onset of the Alpine orogeny). The Ötztal nappe west of the Tauern Window, which occupies a similar structural position as the Ötztal-Bundschuh nappe in the Gurktal Alps, would be an ideal target to further investigations. In contrast, units at low structural levels and closer to the Adriatic indenter, such as the Radenthein/Millstatt Complexes and crustal blocks south of the Tauern Window, have recorded phases of relatively rapid exhumation during the Eocene and since the Miocene, respectively. Whether the counterparts of the Radenthein/Millstatt Complexes west of the Tauern Window (i.e., Schneeberg/Texel Complex, Figure 1) experienced a similar exhumation history remains to be investigated. In any case, further thermochronological studies of structurally lower units will allow shedding light on exhumation paths during the transition from oceanic subduction to subsequent continental collision.

With respect to deriving exhumation histories from thermochronological data, our study demonstrates that the combination of cooling ages from closely spaced samples along elevation profiles and thermokinematic inverse modeling of the respective data allows reconstructing cooling and exhumation histories of crustal blocks in continental collision zones in great detail. In contrast to the conventional approach of spatially distributed sampling and thermal modeling of individual samples, thermokinematic modeling allows deriving depth-time information from suites of samples with multiple cooling ages, because it enables to account for temporal changes of the temperature field due to heat advection and thermal relaxation.

## Conflict of Interest

The authors declare no conflicts of interest relevant to this study.

## Data Availability Statement

All the data used in this study can be obtained from the figures, tables, and references. The data contained in Tables 1–5 will be made available on the PANGAEA data repository server (Wölfler et al., 2023; <https://doi.org/10.1594/PANGAEA.954973>), which complies to the FAIR data guidelines.

## Acknowledgments

We thank the Associate Editor E. Willingshofer and the reviewers C. Rosenberg and P. Eizenhöfer for their constructive reviews that improved the manuscript. C. Meyer (Hannover) is thanked for her help with sample preparation and mineral separation. Open Access funding enabled and organized by Projekt DEAL.

## References

- Behrmann, J. H. (1988). Crustal-scale extension in a convergent orogeny: The Sterzing-Steinach mylonite zone in the Eastern Alps. *Geodinamica Acta*, 2, 63–73. <https://doi.org/10.1080/09853111.1988.1105157>
- Bernet, M., Brandon, M., Graver, J., Balestieri, M. L., Ventura, B., & Zattin, M. (2009). Exhuming the Alps through time: Clues from detrital zircon fission-track thermochronology. *Basin Research*, 21(6), 781–798. <https://doi.org/10.1111/j.1365-2117.2009.00400.x>
- Bertrand, A., Rosenberg, C., Rabaut, A., Herman, F., & Fügenschuh, B. (2017). Exhumation mechanisms of the Tauern Window (Eastern Alps) inferred from apatite and zircon fission track thermochronology. *Tectonics*, 36(2), 207–228. <https://doi.org/10.1002/2016tc004133>
- Braun, J., van der Beek, P., Valla, P., Robert, X., Herman, F., Glotzbach, C., et al. (2012). Quantifying rates of landscape evolution and tectonic processes by thermochronology and numerical modeling of crustal heat transport using PECUBE. *Tectonophysics*, 524–525, 1–28. <https://doi.org/10.1016/j.tecto.2011.12.035>
- Burchfiel, B. C. (1982). Eastern European Alpine system and the Carpathian orocline as an example of collision tectonics. *Tectonophysics*, 63(1–4), 31–61. [https://doi.org/10.1016/0040-1951\(80\)90106-7](https://doi.org/10.1016/0040-1951(80)90106-7)
- Burtner, R., Nigrini, A., & Doneleck, R. A. (1994). Thermochronology of lower cretaceous source rocks in the Idaho-Wyoming thrust belt. *Bulletin of the American Association of Petroleum Geologists*, 78, 1613–1636.
- Butler, R. W. H. (1986). Thrust tectonics, deep structure and crustal subduction in the Alps and Himalayas. *Journal of the Geological Society*, 143(6), 857–873. <https://doi.org/10.1144/gsjgs.143.6.0857>
- Caporali, A., Aichhorn, C., Barlik, M., Becker, M., Fejes, I., Gerhatova, L., et al. (2009). Surface kinematics in the Alpine-Carpathian-Dinaric and Balkan region inferred from a new multi-network GPS combination solution. *Tectonophysics*, 474(1–2), 295–321. <https://doi.org/10.1016/j.tecto.2009.04.035>
- Coyle, D. (1994). *The application of apatite fission track analysis to problems in tectonics* (p. 258). Unpublished Ph.D. thesis. La Trobe University Australia.
- Dallmeyer, R. D., Neubauer, F., Handler, R., Fritz, H., Müller, W., Pana, D., et al. (1996). Tectonothermal evolution of the internal Alps and Carpathians: Evidence from  $^{40}\text{Ar}/^{39}\text{Ar}$  mineral and whole rock data. *Eclogae Geologicae Helvetiae*, 89, 203–227.
- Deutsch, A. (1984). Young alpine dykes south of the Tauern window (Austria): A K-Ar and Sr isotope study. *Contributions to Mineralogy and Petrology*, 85(1), 45–57. <https://doi.org/10.1007/bf00380220>
- Dewey, J. F. (1988). Extensional collapse of orogens. *Tectonics*, 7(6), 1123–1139. <https://doi.org/10.1029/TC007i006p01123>
- Di Fiore, G. (2013). *Evoluzione Morfotettonica Delle aree alpine "Sempione" E "Brennero" Attraverso Studi Termocronologici Di Bassa Temperatura*. Unpublished Ph.D. thesis. Università di Bologna (p. 122).

- Dingeldey, C., Dallmeyer, R. D., Koller, F., & Massonne, H.-J. (1997). P-T-t history of the lower Austroalpine nappe complex in the "Tarntaler Berge" NW of the Tauern window: Implications for the geotectonic evolution of the central eastern Alps. *Contributions to Mineralogy and Petrology*, 129, 1–19. <https://doi.org/10.1007/s004100050319>
- Donelick, R. A., Ketcham, R. A., & Carlson, W. D. (1999). Variability of apatite fission track annealing kinetics II: Crystallographic orientation effects. *American Mineralogist*, 84(9), 1224–1234. <https://doi.org/10.2138/am-1999-0902>
- Dunkl, I. (2002). Trackkey: A windows program for calculation and graphical presentation of fission track data. *Computers and Geosciences*, 28(1), 3–12. [https://doi.org/10.1016/s0098-3004\(01\)00024-3](https://doi.org/10.1016/s0098-3004(01)00024-3)
- Dunkl, I., & Demény, A. (1997). Exhumation of the Rechnitz window at the border of the eastern Alps and Pannonian basin during Neogene extension. *Tectonophysics*, 272(2–4), 197–211. [https://doi.org/10.1016/s0040-1951\(96\)00258-2](https://doi.org/10.1016/s0040-1951(96)00258-2)
- Dunkl, I., Frisch, W., & Grundmann, G. (2003). Zircon fission track thermochronology of the southeastern part of the Tauern Window and the adjacent Austroalpine margin, Eastern Alps. *Elogiae Geologicae Helvetiae*, 96, 209–201.
- Dunkl, I., Kuhlemann, J., Reinecker, J., & Frisch, W. (2005). Cenozoic relief evolution of the Eastern Alps – Constraints from apatite fission track age-provenance of Neogene intramontane sediments. *Austrian Journal of Earth Sciences*, 98, 92–105.
- Eizenhöfer, P. R., Glotzbach, C., Büttner, L., Kley, J., & Ehlers, T. A. (2021). Turning the orogenic switch: Slab-reversal in the Eastern Alps recorded by low-temperature thermochronology. *Geophysical Research Letters*, 48(6), e2020GL092121. <https://doi.org/10.1029/2020gl092121>
- Eizenhöfer, P. R., Glotzbach, C., Kley, J., & Ehlers, T. A. (2023). Thermo-kinematic evolution of the eastern European Alps along the TRANSALP transect. *Tectonics*, 42, e2022TC007380. <https://doi.org/10.1029/2022TC007380>
- Elias, J. (1998). The thermal history of the Ötztal-Stubai complex (Tyrol, Austria/Italy) in the light of the lateral extrusion model. *Tübinger Geowissenschaftliche Arbeiten, Reihe A, Band*, 42, 172.
- Emmermann, R., & Lauterjung, J. (1997). The German continental deep drilling program KTB: Overview and major results. *Journal of Geophysical Research*, 102(B8), 18179–18201. <https://doi.org/10.1029/96jb03945>
- England, P., & Molnar, P. (1990). Surface uplift, uplift of rocks, and exhumation of rocks. *Geology*, 18(12), 1173–1177. [https://doi.org/10.1130/0091-7613\(1990\)018<1173:suora>2.3.co;2](https://doi.org/10.1130/0091-7613(1990)018<1173:suora>2.3.co;2)
- Farley, K. A. (2000). Helium diffusion from apatite: General behavior as illustrated by Durango fluorapatite. *Journal of Geophysical Research*, 105(B2), 2903–2914. <https://doi.org/10.1029/1999jb900348>
- Farley, K. A. (2002). (U-Th)/He dating: Techniques, calibrations and applications. *Mineralogical Society of America Reviews in Mineralogy and Geochemistry*, 47(1), 819–844. <https://doi.org/10.2138/rmg.2002.47.18>
- Farley, K. A., Wolf, R. A., & Silver, L. T. (1996). The effects of long alpha-stopping distances on (U-Th) / He ages. *Geochimica et Cosmochimica Acta*, 60(21), 4223–4229. [https://doi.org/10.1016/0016-7037\(96\)00193-7](https://doi.org/10.1016/0016-7037(96)00193-7)
- Faupl, P., Prober, E., & Wagreich, M. (1987). Facies development of the Gosau Group of the eastern parts of the northern calcareous Alps during the cretaceous and Paleogene. In H. W. Flügel & P. Faupl (Eds.), *Geodynamics of the Eastern Alps* (pp. 142–155). Deuticke.
- Faupl, P., & Wagreich, M. (2000). Late Jurassic to Eocene paleogeography and geodynamic evolution of the Eastern Alps. *Mitteilungen der Österreichischen Geologischen Gesellschaft*, 92, 79–94.
- Favaro, S., Handy, M. R., Scharf, A., & Schuster, R. (2017). Changing patterns of exhumation and denudation in front of an advancing crustal indenter, Tauern Window (Eastern Alps). *Tectonics*, 36(6), 1053–1071. <https://doi.org/10.1002/2016tc004448>
- Favaro, S., Schuster, R., Handy, A., Scharf, A., & Pestal, G. (2015). Transition from orogen-perpendicular to orogen-parallel exhumation and cooling during crustal indentation – Key constraints from  $^{147}\text{Sm}/^{144}\text{Nd}$  and  $^{87}\text{Rb}/^{87}\text{Sr}$  geochronology (Tauern Window, Alps). *Tectonophysics*, 665, 1–16. <https://doi.org/10.1016/j.tecto.2015.08.037>
- Flisch, M. (1986). Die Hebungs geschichte der oberostalpinen Silvretta-Decke seit der mittleren Kreide. *Bulletin der Vereinigung Schweizer Petroleum-Geologen und Ingenieure*, 52(123), 23–51.
- Fodor, L. I., Csontos, L., Bada, G., Györfi, I., & Benkovics, L. (1999). Tertiary tectonic evolution of the Pannonian Basin and neighbouring orogens: A new synthesis of palaeostress data. In B. Durand, L. Jolivet, F. Horváth, & M. Séranne (Eds.), *The Mediterranean basins: Tertiary extension within the alpine orogen* (Vol. 156, pp. 295–334). Geological Society London Special Publications.
- Fodor, L. I., Gerdes, A., Dunkl, I., Koroknai, K., Péskay, Z., Trajanova, M., et al. (2008). Miocene emplacement and rapid cooling of the Pohorje pluton at the Alpine-Pannonian-Dinaridic junction: A geochronological and structural study. *Swiss Journal of Geosciences*, 101(1), 255–271. <https://doi.org/10.1007/s00015-008-1286-9>
- Foeken, J. P. T., Persano, C., Stuart, F. M., & Vooerde, T. M. (2007). Role of topography in isotherm perturbation: Apatite (U-Th)/He and fission track results from the Malta Tunnel, Tauern window, Austria. *Tectonics*, 26(3), TC3006. <https://doi.org/10.1029/2006TC002049>
- Frank, W., Kralik, S., Scharbert, S., & Thöni, M. (1987). Geochronological data from the Eastern Alps. In H. W. Flügel & P. Faupl (Eds.), *Geodynamics of the Eastern Alps* (pp. 272–281). Deuticke.
- Frisch, W., Dunkl, I., & Kuhlemann, J. (2000). Post-collisional orogen-parallel large-scale extension in the Eastern Alps. *Tectonophysics*, 327(3–4), 239–265. [https://doi.org/10.1016/s0040-1951\(00\)00204-3](https://doi.org/10.1016/s0040-1951(00)00204-3)
- Frisch, W., Kuhlemann, J., Dunkl, I., & Brügl, A. (1998). Palinspastic reconstruction and topographic evolution of the Eastern Alps during late Tertiary tectonic extrusion. *Tectonophysics*, 297(1–4), 1–15. [https://doi.org/10.1016/s0040-1951\(98\)00160-7](https://doi.org/10.1016/s0040-1951(98)00160-7)
- Frisch, W., Székely, B., Kuhlemann, J., & Dunkl, I. (2000). Geomorphological evolution of the Eastern Alps in response to Miocene tectonics. *Zeitschrift für Geomorphologie*, 44(1), 103–138. <https://doi.org/10.1127/zg/44/2000/103>
- Froitzheim, N., Conti, P., & van Daalen, M. (1997). Late Cretaceous, synorogenic, low-angle normal faulting along the Schlinig fault (Switzerland, Italy, Austria) and its significance for the tectonics of the Eastern Alps. *Tectonophysics*, 280(3–4), 267–293. [https://doi.org/10.1016/s0040-1951\(97\)00037-1](https://doi.org/10.1016/s0040-1951(97)00037-1)
- Froitzheim, N., Schmid, S. M., & Conti, P. (1994). Repeated change from crustal shortening to orogen-parallel extension in the Austroalpine units of Graubünden. *Elogiae Geologicae Helvetiae*, 87(2), 559–612.
- Fügenschuh, B. (1995). *Thermal and kinematic history of the Brenner area (eastern Alps, Tyrol)* (p. 224). Ph.D. thesis, ETH Zurich.
- Fügenschuh, B., Mancktelow, N. S., & Schmid, S. M. (2012). Comment on Rosenberg and Garcia, 2011: Estimating displacement along the Brenner Fault and orogen-parallel extension in the Eastern Alps. *International Journal of Earth Sciences*, 101(5), 1451–1455. <https://doi.org/10.1007/s00531-011-0725-4>
- Fügenschuh, B., Mancktelow, N. S., & Seward, D. (2000). The cretaceous to Neogene cooling and exhumation history of the Oetztal-Stubai basement complex, eastern Alps: A structural and fission-track study. *Tectonics*, 19(5), 905–918. <https://doi.org/10.1029/2000tc900014>
- Fügenschuh, B., Seward, D., & Mancktelow, N. (1997). Exhumation in a convergent orogeny: The western Tauern window. *Terra Nova*, 9, 2132.
- Galbraith, F. G., & Laslett, G. M. (1993). Statistical models for mixed fission track ages. *Nuclear Tracks and Radiation Measurements*, 21(4), 459–470. [https://doi.org/10.1016/1359-0189\(93\)90185-c](https://doi.org/10.1016/1359-0189(93)90185-c)
- Gallagher, K. (2012). Transdimensional inverse thermal history modeling for quantitative thermochronology. *Journal of Geophysical Research*, 117(B2), B02408. <https://doi.org/10.1029/2011JB008825>

- Gebrände, H., Lüschen, E., Bopp, M., Bleibinhaus, F., Lammerer, B., Oncken, O., et al. (2002). First deep seismic reflection images of the Eastern Alps reveal giant crustal wedges and transcurrent ramps. *Geophysical Research Letters*, 29(10), 92-1–92-4. <https://doi.org/10.1029/2002gl014911>
- Genser, J., & Neubauer, F. (1989). Low angle normal faults at the eastern margin of the Tauern window (Eastern Alps). *Mitteilungen der Österreichischen Geologischen Gesellschaft*, 81, 233–243.
- Gleadow, A. J. W. (1981). Fission-track dating methods: What are the real alternatives? *Nuclear Tracks*, 5(1–2), 3–14. [https://doi.org/10.1016/0191-278x\(81\)90021-4](https://doi.org/10.1016/0191-278x(81)90021-4)
- Glogny, J., Ring, U., Kühn, A., Gleissner, P., & Franz, G. (2005). Crystallization and very rapid exhumation of the youngest Alpine eclogites (Tauern Window, Eastern Alps) from Rb/Sr mineral assemblage analysis. *Contributions to Mineralogy and Petrology*, 149(6), 699–712. <https://doi.org/10.1007/s00410-005-0676-5>
- Griesmeier, E. U., Schuster, R., & Grasemann, B. (2018). Major fault zones in the Austroalpine units of the Kreuzeck mountains south of the Tauern window (Eastern Alps, Austria). *Swiss Journal of Geosciences*, 112(1), 39–53. <https://doi.org/10.1007/s00015-018-0328-1>
- Groß, P., Handy, M. R., John, T., Pestal, G., & Pleuger, J. (2020). Crustal-scale sheath folding at HP conditions in an exhumed Alpine subduction zone (Tauern Window, Eastern Alps). *Tectonics*, 39, e2019TC005942. <https://doi.org/10.1029/2019TC005942>
- Grundmann, G., & Morteani, G. (1985). The young uplift and thermal history of the Central Alps (Austria/Italy), evidence from apatite fission track ages. *Jahrbuch der Geologischen Bundesanstalt*, 128, 197–216.
- Guenther, W. R. (2021). Implementation of an alpha damage annealing model for zircon (U-Th)/He thermochronology with comparison to a zircon fission track annealing model. *Geochemistry, Geophysics, Geosystems*, 22(2), e2019GC008757. <https://doi.org/10.1029/2019GC008757>
- Guenther, W. R., Reiners, P. W., Ketcham, R. A., Nasdala, L., & Gieser, G. (2013). Helium diffusion in natural zircon: Radiation damage, anisotropy, and the interpretation of zircon (U-Th)/He thermochronology. *American Journal of Science*, 313(3), 145–198. <https://doi.org/10.2475/03.2013.01>
- Handy, M. R., Schmid, S. M., Bousquet, R., Kissling, E., & Bernoulli, D. (2010). Reconciling plate-tectonic reconstructions with the geological-geophysical record of spreading and subduction in the Alps. *Earth-Science Reviews*, 102, 121–158.
- Handy, M. R., Ustaszewski, K., & Kissling, E. (2015). Reconstructing the Alps-Carpathians-Dinarides as a key to understanding switches in subduction polarity, slab gaps and surface motion. *International Journal of Earth Sciences*, 104, 1–16. <https://doi.org/10.1007/s00531-014-1060-3>
- Heberer, B., Revermann, R. L., Fellin, M. G., Neubauer, F., Dunkl, I., Zattin, M., et al. (2016). Postcollisional cooling history of the eastern and southern Alps and its linkage to Adria indentation. *International Journal of Earth Sciences*, 106(5), 1557–1580. <https://doi.org/10.1007/s00531-016-1367-3>
- Hejl, E. (1997). "Cold spots" during cenozoic evolution of the eastern Alps: Thermochronological interpretation of apatite fission track data. *Tectonophysics*, 272(2–4), 159–173. [https://doi.org/10.1016/s0040-1951\(96\)00256-9](https://doi.org/10.1016/s0040-1951(96)00256-9)
- Hejl, E. (1998). Über die känozoische Abkühlung und Denudation der Zentralalpen östlich der Hohen Tauern: Eine Apatit-Spaltspurenanalyse. *Mitteilungen der Österreichischen Geologischen Gesellschaft*, 89, 179–200.
- Hejl, E., & Grundmann, G. (1989). Apatit-Spaltspurendaten zur thermischen Geschichte der Nördlichen Kalkalpen, der Flysch- und Molassezone. *Jahrbuch der Geologischen Bundesanstalt*, 132(1), 191–212.
- Henk, A. (1997). Gravitational orogenic collapse vs plate-boundary stresses: A numerical modelling approach to the Permo-carboniferous evolution of central Europe. *Geologische Rundschau*, 86(1), 39–55. <https://doi.org/10.1007/s005310050120>
- Hoinkes, G., Koller, F., Rantitsch, G., Dachs, E., Höck, V., Neubauer, F., et al. (1999). Alpine metamorphism of the eastern Alps. *Schweizerische Mineralogische und Petrographische Mitteilungen*, 79, 155–181.
- Hoke, L. (1990). The Altkristallin of the Kreuzeck mountains, SE Tauern window, eastern Alps; basement crust in a convergent plate boundary zone. *Jahrbuch der Geologischen Bundesanstalt Wien*, 133, 5–87.
- Hourigan, J., Reiners, P. W., & Brandon, M. T. (2005). U-Th zonation-dependent alpha-ejection in (U-Th)/He chronometry. *Geochimica et Cosmochimica Acta*, 69(13), 3349–3365. <https://doi.org/10.1016/j.gca.2005.01.024>
- Hülscher, J., Sobel, E. R., Verwater, V., Groß, P., Chew, C., & Bernhardt, A. (2021). Detrital apatite geochemistry and thermochronology from the Oligocene/Miocene Alpine foreland record the early exhumation of the Tauern Window. *Basin Research*, 33(6), 3021–3044. <https://doi.org/10.1111/bre.12593>
- Hurford, A. J. (1991). Uplift and cooling pathways derived from fission track analysis and mica dating: A review. *Geologische Rundschau*, 80(2), 449–368. <https://doi.org/10.1007/bf01829371>
- Hurford, A. J., & Green, P. F. (1983). The zeta age calibration of fission-track dating. *Chemical Geology*, 1, 285–317. [https://doi.org/10.1016/s0009-2541\(83\)80026-6](https://doi.org/10.1016/s0009-2541(83)80026-6)
- Igliseder, C. (2019). *Geologische und Tektonische Karte der Gurktaler Alpen 1:250 000* (pp. 48–54). Arbeitstagung der Geologischen Bundesanstalt.
- Kaindl, R., & Abart, R. (2002). Reequilibration of fluid inclusions in garnet and kyanite from metapelites of the Radenthein Complex, Austroalpine Basement, Austria. *Schweizerische Mineralogische und Petrographische Mitteilungen*, 82, 467–486.
- Kázmér, M., Dunkl, I., Frisch, W., Kuhlemann, J., & Ozsvárt, P. (2003). The Palaeogene forearc basin of the eastern Alps and western carpathians: Subduction erosion and basin evolution. *Journal of the Geological Society London*, 160(3), 413–428. <https://doi.org/10.1144/0016-764902-041>
- Ketcham, R. A. (2005). Forward and inverse modeling of low-temperature thermochronometry data. In P. Reiners & T. A. Ehlers (Eds.) (Vol. 58, pp. 275–314). *Low-temperature thermochronology: Techniques, interpretations, and applications*. *Reviews in Mineralogy & Geochemistry*.
- Klug, L., & Froitzheim, N. (2022). Reuniting the Ötztal nappe: The tectonic evolution of the Schneeberg complex. *International Journal of Earth Sciences*, 111(2), 535–542. <https://doi.org/10.1007/s00531-021-02127-4>
- Koroknai, B., Neubauer, F., Genser, J., & Topa, D. (1999). Metamorphic and tectonic evolution of Austroalpine units at the western margin of the Gurktal nappe complex, Eastern Alps. *Schweizerische Mineralogische und Petrographische Mitteilungen*, 79, 277–295.
- Krämer, K. (1984). Sedimentologische Untersuchungen an permischen und untertriadischen Sedimenten des Stangalm-Mesozoikums (Kärnten/Österreich). *Jahrbuch der Geologischen Bundesanstalt*, 127, 159–179.
- Krenn, K., Fritz, H., Mogessi, A., & Schaflechner, J. (2008). Late cretaceous exhumation history of an extensional extruding wedge (Graz Paleozoic nappe complex, Austria). *International Journal of Earth Sciences*, 97(6), 1331–1352. <https://doi.org/10.1007/s00531-007-0221-z>
- Krenn, K., Kurz, W., Fritz, H., & Hoinkes, G. (2011). Eoalpine tectonics of the Eastern Alps: Implications from the evolution of monometamorphic Austroalpine units (Schneeberg and Radenthein complex). *Swiss Journal of Geosciences*, 104(3), 471–491. <https://doi.org/10.1007/s00015-011-0087-8>
- Krohe, A. (1987). Kinematics of Cretaceous nappe tectonics in the Austroalpine basement of the Koralpe region (eastern Austria). *Tectonophysics*, 136(3–4), 171–196. [https://doi.org/10.1016/0040-1951\(87\)90024-2](https://doi.org/10.1016/0040-1951(87)90024-2)
- Kuhlemann, J., Frisch, W., Székely, B., Dunkl, I., & Kázmér, M. (2002). Post-collisional sediment budget history of the Alps: Tectonic versus climatic control. *International Journal of Earth Sciences*, 91(5), 818–837. <https://doi.org/10.1007/s00531-002-0266-y>

- Kuhlemann, J., & Kempf, O. (2002). Post-eocene evolution of the north alpine foreland basin and its response to alpine tectonics. *Sedimentary Geology*, 152(1–2), 45–78. [https://doi.org/10.1016/s0037-0738\(01\)00285-8](https://doi.org/10.1016/s0037-0738(01)00285-8)
- Kuhlemann, J., Taubald, H., Vennemann, T., Dunkl, I., & Frisch, W. (2008). Clay mineral and geochemical composition of Cenozoic paleosol in the Eastern Alps (Austrian). *Austrian Journal of Earth Sciences*, 101, 60–69.
- Kurz, W., & Fritz, H. (2003). Tectonometamorphic evolution of the Austroalpine nappe complex in the central Eastern Alps – Consequences for the eo-Alpine evolution of the Eastern Alps. *International Geology Review*, 45(12), 100–127. <https://doi.org/10.2747/0020-6814.45.12.1100>
- Kurz, W., Fritz, H., Tenczer, V., & Unzog, W. (2002). Tectonometamorphic evolution of the Koralpe complex (Eastern Alps): Constraints from microstructures and textures of the “Plattengneis” shear zone. *Tectonophysics*, 388(1–4), 1957–1970. [https://doi.org/10.1016/s0040-8088\(02\)00008-1](https://doi.org/10.1016/s0040-8088(02)00008-1)
- Kurz, W., Handler, R., & Bertoldi, C. (2008). Tracing the exhumation of the eclogite zone (Tauern window, eastern Alps) by  $^{40}\text{Ar}/^{39}\text{Ar}$  dating of white mica in eclogites. *Swiss Journal of Geosciences*, 101(1), 191–206. <https://doi.org/10.1007/s00015-008-1281-1>
- Laubscher, H. P. (1983). The late alpine (Periadriatic) intrusions and the Insubric line. *Memorie della Società Geologica Italiana*, 26, 21–30.
- Legrain, N., Stüwe, K., & Wölfle, A. (2014). Incised relict landscape in the eastern Alps. *Geomorphology*, 221, 124–138. <https://doi.org/10.1016/j.geomorph.2014.06.010>
- Lemcke, K. (1988). Das Bayrische Alpenvorland vor der Eiszeit. Erdgeschichte-Bau-Bodenschätz. *E. Schweizerbart'sche Verlagsbuchhandlung (Nägele & Obermiller)*, 175.
- Linzer, H.-G., Decker, K., Peresson, H., Dell'Mour, R., & Frisch, W. (2002). Balancing orogenic float of the Eastern Alps. *Tectonophysics*, 354(3–4), 211–237. [https://doi.org/10.1016/s0040-1951\(02\)00337-2](https://doi.org/10.1016/s0040-1951(02)00337-2)
- Liu, Y., Genser, J., Handler, R., Friedl, G., & Neubauer, F. (2001).  $^{40}\text{Ar}/^{39}\text{Ar}$  muscovite ages from the Penninic-Austroalpine plate boundary, Eastern Alps. *Tectonics*, 20(4), 526–547. <https://doi.org/10.1029/2001tc900011>
- Lüschen, E., Lammerer, B., Gebrannde, H., Millahn, K., & Nicolich, R., & TRANSALP Working Group. (2004). Orogenic structure of the Eastern Alps, Europe, from Transalp deep seismic reflection profiling. *Tectonophysics*, 388(1–4), 85–102. <https://doi.org/10.1016/j.tecto.2004.07.024>
- Luth, S., & Willingshofer, E. (2008). Mapping of the post-collisional history of the Eastern Alps. *Swiss Journal of Geosciences*, 101(1), 207–223. <https://doi.org/10.1007/s00015-008-1294-9>
- Mancktelow, N. S. (1992). Neogene lateral extension during convergence in the central Alps: Evidence from interrelated faulting and backfolding around the Simpionpass (Switzerland). *Tectonophysics*, 215(3–4), 295–317. [https://doi.org/10.1016/0040-1951\(92\)90358-d](https://doi.org/10.1016/0040-1951(92)90358-d)
- Mancktelow, N. S., Stöckli, D. F., Grollmund, B., Müller, W., Fügenschuh, B., Viola, G., et al. (2001). The DAV and Periadriatic Fault systems in the eastern Alps south of the Tauern window. *International Journal of Earth Sciences*, 90(3), 593–622. <https://doi.org/10.1007/s005310000190>
- Mandl, G. W. (2000). The alpine sector of the Tethyan shelf – Examples of Triassic to Jurassic sedimentation and deformation from the northern calcareous Alps. *Mitteilungen der Österreichischen Geologischen Gesellschaft*, 92, 61–78.
- Martin, S., Bigazzi, G., Zattin, M., Viola, G., & Balestrieri, M. L. (1998). Neogene kinematics of the Giudicarie fault (Central-Eastern Alps, Italy): New apatite fission-track data. *Terra Nova*, 10(4), 217–221. <https://doi.org/10.1046/j.1365-3121.1998.00119.x>
- Miladinova, I., Froitzheim, N., Nagel, T. J., Janak, M., Fonseca, R. O. C., Sprung, P., & Münter, C. (2022). Constraining the process of intracontinental subduction in the Austroalpine Nappes: Implications from petrology and Lu-Hf geochronology of eclogites. *Journal of Metamorphic Geology*, 40(3), 423–456. <https://doi.org/10.1111/jmg.12634>
- Molnar, P., England, P., & Martinod, J. (1993). Mantle dynamics, uplift of the Tibetan Plateau, and the Indian Monsoon. *Reviews of Geophysics*, 31(4), 357–396. <https://doi.org/10.1029/93rg02030>
- Molnar, P., & Lyon-Caen, H. (1988). Some simple Physical aspects of the support, structure and evolution of mountain belts. *Geological Society of America Special Paper*, 218, 179–207.
- Most, P. (2003). Late alpine cooling histories of tectonic blocks along the central part of the TRANSALP-traverse (Inntal - Gadertal): Constraints from geochronology. *Tübinger Geowissenschaftliche Arbeiten, Reihe A*, 67, 97.
- Müller, W., Mancktelow, N. S., & Meier, M. (2000). Rb-Sr microchrons of synkinematic mica in mylonites: An example from the DAV fault of the eastern Alps. *Earth and Planetary Science Letters*, 180(3–4), 385–397. [https://doi.org/10.1016/s0012-821x\(00\)00167-9](https://doi.org/10.1016/s0012-821x(00)00167-9)
- Naeser, C. W. (1978). Fission track dating. U.S. Geological Survey Open File Report, (pp. 76–190).
- Nagel, T. J., Herwartz, D., Rexroth, S., Münter, C., Froitzheim, N., & Kurz, W. (2013). Lu-Hf dating, petrography, and tectonic implications of the youngest Alpine eclogites (Tauern Window, Austria). *Lithos*, 170–171, 179–190. <https://doi.org/10.1016/j.lithos.2013.02.008>
- Neubauer, F., Dallmeyer, R. D., Dunkl, I., & Schirnuk, D. (1995). Late cretaceous exhumation of the metamorphic Gleinalm dome, Eastern Alps: Kinematics, cooling history and sedimentary response in a sinistral wrench corridor. *Tectonophysics*, 242(1–2), 79–98. [https://doi.org/10.1016/0040-1951\(94\)00154-2](https://doi.org/10.1016/0040-1951(94)00154-2)
- Neubauer, F., Genser, J., & Handler, R. (2000). The Eastern Alps: Result of a two-stage collision process. *Mitteilungen der Österreichischen Geologischen Gesellschaft*, 92, 117–134.
- Neubauer, F., Genser, J., & Handler, R. (2003). Tectonic evolution of the western margin of the Gurktal nappe complex, Eastern Alps: Constraints from structural studies and  $^{40}\text{Ar}/^{39}\text{Ar}$ /white mica ages. *Mitteilungen der Österreichischen Mineralogischen Gesellschaft*, 148, 240–241.
- Neubauer, F., Genser, J., Kurz, W., & Wang, X. (1999). Exhumation of the Tauern window; Eastern Alps. *Physics and Chemistry of the Earth*, 24(8), 675–680. [https://doi.org/10.1016/s1464-1895\(99\)00098-8](https://doi.org/10.1016/s1464-1895(99)00098-8)
- Oberhänsli, R. (2004). Metamorphic structure of the Alps. *Mitteilungen der Österreichischen Mineralogischen Gesellschaft*, 149, 115–226.
- Oberhauser, R. (1995). Zur Kenntnis der Tektonik und der Paläogeographie des Ostalpenraumes zur Kreide-, Paläozän-, und Eozänzeit. *Jahrbuch der Geologischen Bundesanstalt*, 138(2), 369–432.
- Ortner, H., Aichholzer, S., Zerlauth, M., Pilser, R., & Fügenschuh, B. (2015). Geometry, amount, and sequence of thrusting in the Subalpine Molasse of western Austria and southern Germany, European Alps. *Tectonics*, 34, 1–30. <https://doi.org/10.1002/2014tc003550>
- Pfiffner, A. (2009). *Geologie der Alpen* (p. 359pp). HauptVerlag.
- Pfingstl, S., Kurz, W., Schuster, R., & Hauenberger, C. (2015). Geochronological constraints on the exhumation of the Austroalpine Seckau nappe (eastern Alps). *Austrian Journal of Earth Sciences*, 108(1), 172–185. <https://doi.org/10.17738/ajes.2015.0011>
- Polinski, R. K., & Eibacher, H. (1992). Deformation partitioning during polyphase oblique convergence in the Karawanken Mountains, south-eastern Alps. *Journal of Structural Geology*, 14(10), 1203–1213. [https://doi.org/10.1016/0191-8141\(92\)90070-d](https://doi.org/10.1016/0191-8141(92)90070-d)
- Pomella, H., Klötzli, U., Scholger, R., Stipp, M., & Fügenschuh, B. (2010). The Northern Giudicarie and the Meran-Mauls fault (Alps, Northern Italy) in the light of new paleomagnetic and geochronological data from boudinaged Eo-/Oligocene tonalities. *International Journal of Earth Sciences*, 100(8), 1827–1850. <https://doi.org/10.1007/s00531-010-0612-4>
- Pomella, H., Stipp, M., & Fügenschuh, B. (2012). Thermochronological record of thrusting and strike-slip faulting along the Giudicarie fault system (Alps, Northern Italy). *Tectonophysics*, 579, 118–130. <https://doi.org/10.1016/j.tecto.2012.04.015>

- Rantitsch, G., Iglseder, C., Schuster, R., Hollinetz, M. S., Huet, B., & Werdenich, M. (2020). Organic metamorphism as key for reconstructing tectonic processes: A case study from the Austroalpine unit (Eastern Alps). *International Journal of Earth Sciences*, 109(6), 2235–2253. <https://doi.org/10.1007/s00531-020-01897-7>
- Rantitsch, G., & Russegger, B. (2000). Thrust-related very low grade metamorphism within the Gurktal nappe complex (Eastern Alps). *Jahrbuch der Geologischen Bundesanstalt*, 142, 2192.
- Rantitsch, G., Sachsenhofer, R. F., Hasenhüttl, C., Russegger, B., & Rainer, T. (2005). Thermal evolution of an extensional detachment as constrained by organic metamorphic data and thermal modelling: Graz Paleozoic Nappe Complex (Eastern Alps). *Tectonophysics*, 411(1–4), 57–72. <https://doi.org/10.1016/j.tecto.2005.08.022>
- Ratschbacher, L., Dingeldey, C., Miller, C., Hacker, B. R., & McWilliams, M. O. (2004). Formation, subduction, and exhumation of Penninic oceanic crust in the Eastern Alps: Time constraints from  $^{40}\text{Ar}/^{39}\text{Ar}$  geochronology. *Tectonophysics*, 394(3–4), 155–170. <https://doi.org/10.1016/j.tecto.2004.08.003>
- Ratschbacher, L., Frisch, W., Linzer, H. G., & Merle, O. (1991). Lateral extrusion in the Eastern Alps, part 2: Structural analysis. *Tectonics*, 10(2), 257–271. <https://doi.org/10.1029/90tc02623>
- Ratschbacher, L., Frisch, W., Neubauer, F., Schmid, S. M., & Neugebauer, J. (1989). Extension in compressional orogenic belts: The Eastern Alps. *Geology*, 17(5), 404–407. [https://doi.org/10.1130/0091-7613\(1989\)017<404:eicobt>2.3.co;2](https://doi.org/10.1130/0091-7613(1989)017<404:eicobt>2.3.co;2)
- Ratschbacher, L., Merle, O., Davy, P., & Cobbold, P. (1991). Lateral extrusion in the Eastern Alps, part 1: Boundary conditions and experiments scaled for gravity. *Tectonics*, 10(2), 245–256. <https://doi.org/10.1029/90tc02622>
- Ratschbacher, L., & Neubauer, F. (1989). West-directed décollement of Austro-Alpine cover nappes in the Eastern Alps. *Geological Society, London, Special Publications*, 45(1), 243–262. <https://doi.org/10.1144/gsl.sp.1989.045.01.14>
- Reinecker, J. (2000). Stress and deformation. Miocene to present-day tectonics in the Eastern Alps. *Tübinger Geowissenschaftliche Arbeiten*, 55, 78.
- Reiners, P. W. (2005). Zircon (U-Th)/He thermochronometry. *Reviews in Mineralogy and Geochemistry*, 58(1), 151–179. <https://doi.org/10.2138/rmg.2005.58.6>
- Reiners, P. W., Spell, T. I., Nicolescu, S., & Zanetti, K. (2004). Zircon (U-Th)/He thermochronometry: He diffusion and comparisons with  $^{40}\text{Ar}/^{39}\text{Ar}$  dating. *Geochimica et Cosmochimica Acta*, 68(8), 1857–1887. <https://doi.org/10.1016/j.gca.2003.10.021>
- Ring, U., Brandon, M. T., Willett, S. D., & Lister, G. S. (1999). *Exhumation processes* (Vol. 154, pp. 1–27). Geological Society Special Publication.
- Ring, U., Ratschbacher, L., Frisch, W., Biehler, D., & Kralik, M. (1989). Kinematics of the alpine plate-margin: Structural styles, strain and motion along the Penninic-Austroalpine boundary in the Swiss-Austrian Alps. *Journal of the Geological Society*, 146(5), 835–849. <https://doi.org/10.1144/gsjgs.146.5.0835>
- Romer, R. L., & Siegesmund, S. (2003). Why allanite may swindle about its true age. *Contributions to Mineralogy and Petrology*, 146(3), 297–307. <https://doi.org/10.1007/s00410-003-0494-6>
- Rosenberg, C. L. (2004). Shear zones and magma ascent. A model based on a review of Tertiary magmatism in the Alps. *Tectonics*, 23(3), TC3002. <https://doi.org/10.1029/2003TC001526>
- Rosenberg, C. L., & Berger, A. (2009). On the causes and modes of exhumation and lateral growth of the Alps. *Tectonics*, 28(6), TC6001. <https://doi.org/10.1029/2008TC002442>
- Rosenberg, C. L., Berger, A., Bellahsen, N., & Bousquet, R. (2015). Relating orogen width to shortening, erosion, and exhumation during Alpine collision. *Tectonics*, 34(6), 1306–1328. <https://doi.org/10.1002/2014tc003736>
- Rosenberg, C. L., Brun, J.-P., Cagnard, F., & Gapais, D. (2007). Oblique indentation in the eastern Alps: Insights from laboratory experiments. *Tectonics*, 26(2), TC2003. <https://doi.org/10.1029/2006tc001960>
- Rosenberg, C. L., Brun, J.-P., & Gapais, D. (2004). Indentation of the eastern Alps and the origin of the Tauern window. *Geology*, 32(11), 997–1000. <https://doi.org/10.1130/g20793.1>
- Rosenberg, C. L., & Garcia, S. (2011). Estimating displacement along the Brenner Fault and orogen-parallel extension in the Eastern Alps. *International Journal of Earth Sciences*, 100(5), 1129–1145. <https://doi.org/10.1007/s00531-011-0645-3>
- Rosenberg, C. L., & Garcia, S. (2012). Reply to the comment of Fügenschuh et al. 2012, on the paper ‘estimating displacement along the Brenner Fault and orogen-parallel extension in the Eastern Alps’ by Rosenberg and Garcia, 2011. *International Journal of Earth Sciences*, 101(5), 1457–1464. <https://doi.org/10.1007/s00531-011-0726-3>
- Rosenberg, C. L., & Schneider, S. (2008). The western termination of the SEMP Fault (eastern Alps) and its bearing on the exhumation of the Tauern Window. In S. Siegesmund, B. Fügenschuh, & N. Froitzheim (Eds.), *Tectonic Aspects of the Alpine-Dinaride-Carpathian system* (Vol. 298, pp. 197–218). Geological Society Special Publications.
- Rosenberg, C. L., Schneider, S., Scharf, A., Bertrand, A., Hammerschmidt, K., Rabaute, A., & Brun, J. P. (2018). Relating collisional kinematics to exhumation processes in the Eastern Alps. *Earth-Science Reviews*, 176, 311–344. <https://doi.org/10.1016/j.earscirev.2017.10.013>
- Royden, L. H. (1993). Evolution of retreating subduction boundaries during continental collision. *Tectonics*, 12(3), 629–638. <https://doi.org/10.1029/92tc02641>
- Sachsenhofer, R. F., Kogler, A., Strauss, P., & Wagreich, M. (2000). The Neogene Fohnsdorf basin: Basin formation and basin inversion during lateral extrusion in the Eastern Alps (Austria). *Geologische Rundschau*, 89(2), 415–430. <https://doi.org/10.1007/s005310000083>
- Sachsenhofer, R. F., Lankreijer, A., Cloetingh, S., & Ebner, F. (1997). Subsidence analysis and quantitative basin modelling in the Styrian basin (Pannonian basin system, Austria). *Tectonophysics*, 272(2–4), 175–196. [https://doi.org/10.1016/s0040-1951\(96\)00257-0](https://doi.org/10.1016/s0040-1951(96)00257-0)
- Sambridge, M. (1999a). Geophysical inversion with a neighbourhood algorithm-I. Searching a parameter space. *Geophysical Journal International*, 138(2), 479–494. <https://doi.org/10.1046/j.1365-246x.1999.00876.x>
- Sambridge, M. (1999b). Geophysical inversion with a neighbourhood algorithm-II. Appraising the ensemble. *Geophysical Journal International*, 138(3), 727–746. <https://doi.org/10.1046/j.1365-246x.1999.00900.x>
- Scharf, A., Handy, M. R., Favaro, S., Schmid, S. M., & Bertrand, A. (2013). Modes of orogen-parallel stretching and extensional exhumation in response to microplate indentation and roll-back subduction (Tauern Window, eastern Alps). *International Journal of Earth Sciences*, 102(6), 1627–1654. <https://doi.org/10.1007/s00531-013-0894-4>
- Schmid, S. M., Bernoulli, D., Fügenschuh, B., Matenco, L., Schuster, R., Tischler, M., et al. (2008). The Alpine-carpathian-Dinaridic orogenic system: Correlation and evolution of tectonic units. *Swiss Journal of Geosciences*, 101(1), 139–183. <https://doi.org/10.1007/s00015-008-1247-3>
- Schmid, S. M., Fügenschuh, B., Kissling, E., & Schuster, R. (2004). Tectonic map and overall architecture of the Alpine orogen. *Eclogae Geologicae Helvetiae*, 97(1), 93–117. <https://doi.org/10.1007/s00015-004-1113-x>
- Schmid, S. M., Pfiffner, O. A., Froitzheim, N., Schönborn, G., & Kissling, E. (1996). Geophysical-geological transect and tectonic evolution of the Swiss-Italian Alps. *Tectonics*, 15(5), 1036–1064. <https://doi.org/10.1029/96tc00433>
- Schmid, S. M., Scharf, A., Handy, M. R., & Rosenberg, C. (2013). The Tauern window (eastern Alps, Austria): A new tectonic map, with cross-sections and a tectonometamorphic synthesis. *Swiss Journal of Geosciences*, 106, 1–32. <https://doi.org/10.1007/s00015-013-0123-y>

- Schneider, S., Hammerschmidt, K., Rosenberg, C. L., Gerdes, A., Frei, D., & Bertrand, A. (2015). U-Pb ages of apatite in the western Tauern Window (Eastern Alps): Tracing the onset of collision-related exhumation in the European plate. *Earth and Planetary Science Letters*, 418, 53–65. <https://doi.org/10.1016/j.epsl.2015.02.020>
- Schorn, S., & Stüwe, K. (2016). The Plankogel detachment of the Eastern Alps: Petrological evidence for an orogen-scale extraction fault. *Journal of Metamorphic Geology*, 34(2), 147–166. <https://doi.org/10.1111/jmg.12176>
- Schuster, R. (2003). Das eo-Alpine Ereignis in den Ostalpen: Plattentektonische Situation und interne Struktur des Ostalpinen Kristallins. *Arbeitstagung der Geologischen Bundesanstalt Blatt 148 Brenner, Blatt 175 Sterzing*, 141–159.
- Schuster, R., & Frank, W. (1999). Metamorphic evolution of the Austroalpine units east of the Tauern window: Indications for Jurassic strike slip tectonics. *Mitteilungen der Gesellschaft der Geologie- und Bergbaustudenten in Österreich*, 42, 37–58.
- Schuster, R., Koller, F., Hoeck, V., Hoinkes, G., & Bousquet, R. (2004). Explanatory notes to the map: Metamorphic structure of the Alps – Metamorphic evolution of the Eastern Alps. *Mitteilungen der Österreichischen Mineralogischen Gesellschaft*, 149, 175–199.
- Schuster, R., Kurz, W., Krenn, K., & Fritz, H. (2013). Introduction to the Geology of the Eastern Alps. *Berichte der Geologischen Bundesanstalt Wien*, 99, 121–133.
- Selverstone, J. (1988). Evidence for east-west crustal extension in the eastern Alps: Implications for the unroofing history of the Tauern window. *Tectonics*, 7(1), 87–105. <https://doi.org/10.1029/tc007001p00087>
- Sissingh, W. (1997). Tectonostratigraphy of the north alpine foreland basin: Correlation of tertiary depositional cycles and orogenic phases. *Tectonophysics*, 282(1–4), 223–256. [https://doi.org/10.1016/s0040-1951\(97\)00221-7](https://doi.org/10.1016/s0040-1951(97)00221-7)
- Sörlva, H., Grasemann, B., Thöni, M., Thiede, R., & Habler, G. (2005). The Schneeberg normal fault zone: Normal faulting associated with cretaceous SE-directed extrusion in the eastern Alps (Italy/Austria). *Tectonophysics*, 401(3–4), 143–166. <https://doi.org/10.1016/j.tecto.2005.02.005>
- Staufenberg, H. (1987). Apatite fission-track evidence for postmetamorphic uplift and cooling history of the eastern Tauern Window and the surrounding Austroalpine (Central Eastern Alps, Austria). *Jahrbuch der Geologischen Bundesanstalt*, 130, 571–586.
- Steenken, A., Siegesmund, S., Heinrichs, T., & Fügenschuh, B. (2002). Cooling and exhumation of the Rieserferner Pluton (Eastern Alps, Italy/Austria). *International Journal of Earth Sciences*, 91(5), 799–817. <https://doi.org/10.1007/s00531-002-0260-4>
- Stöckhert, B., Brix, M. R., Kleinschrodt, R., Hurford, A. J., & Wirth, R. (1999). Thermochronometry and the microstructures of quartz – A comparison with experimental flow laws and predictions on the temperature of the brittle-plastic transition. *Journal of Structural Geology*, 21(3), 351–369. [https://doi.org/10.1016/s0191-8141\(98\)00114-x](https://doi.org/10.1016/s0191-8141(98)00114-x)
- Stüwe, K. (2007). *Geodynamics of the lithosphere* (2nd ed., p. 493). Springer.
- Stüwe, K., & Barr, T. D. (1998). On uplift and exhumation during convergence. *Tectonics*, 17(1), 80–88. <https://doi.org/10.1029/97tc02557>
- Stüwe, K., & Schuster, R. (2010). Initiation of subduction in the Alps: Continent or ocean? *Geology*, 38(2), 171–178. <https://doi.org/10.1130/g30528.1>
- Tagami, T., Galbraith, R. F., Yamada, R., & Laslett, G. M. (1998). Revised annealing kinetics of fission tracks in zircon and geological implications. In P. D. van Haute & F. de Corte (Eds.), *Advances in fission-track geochronology* (pp. 99–112). Springer.
- Tappognon, P., & Molnar, P. (1976). Slip-line field theory and large-scale continental tectonics. *Nature*, 264(5584), 319–324. <https://doi.org/10.1038/264319a0>
- Thöni, M. (1999). A review of geochronological data from the Eastern Alps. *Schweizer Mineralogische und Petrographische Mitteilungen*, 79, 209–230.
- Thöni, M. (2006). Dating eclogite-facies metamorphism in the eastern Alps – Approaches, results, interpretations: A review. *Mineralogy and Petrology*, 88(1–2), 123–148. <https://doi.org/10.1007/s00710-006-0153-5>
- Thöni, M., & Müller, C. (1996). Garnet SM-Nd data from the Saualpe and the Koralpe (Eastern Alps, Austria): Chronological and PT constraints on the thermal and tectonic history. *Journal of Metamorphic Geology*, 14(4), 453–466. <https://doi.org/10.1046/j.1525-1314.1996.05995.x>
- Tollmann, A. (1977). *Geologie von Österreich* (Vol. 1, p. 766). Deuticke.
- Tollmann, A. (1986). *Geologie von Österreich* (Vol. 3, p. 718). Deuticke.
- van den Beukel, J. (1992). Some thermomechanical aspects of the subduction of continental lithosphere. *Tectonics*, 11(2), 316–329. <https://doi.org/10.1029/91tc01039>
- van der Beek, P., & Schildgen, T. (2023). Short communication: Age2exhume – A MATLAB/Python script to calculate steady-state vertical exhumation rates from thermochronometric ages and application to the Himalaya. *Geochronology*, 5(1), 35–49. <https://doi.org/10.5194/gchron-5-35-2023>
- van Gelder, I. E., Willingshofer, W., Andriessen, P. A. M., Schuster, R., & Sokoutis, D. (2020). Cooling and vertical motions of crustal wedges prior to, during and after lateral extrusion in the eastern Alps: New field kinematic and fission track data from the Mur-Mürz fault system. *Tectonics*, 39, e2019TC005754. <https://doi.org/10.1029/2019TC005754>
- Viola, G. (2000). *Kinematics and timing of the Periadriatic Fault system in the Giudicarie region (Central-Eastern Alps)* (p. 205). Unpublished Ph.D. thesis. ETH Zurich.
- Viola, G., Mancktelow, N. S., & Seward, D. (2001). Late Oligocene–Neogene evolution of Europe–Adria collision: New structural and geochronological evidence from the Giudicarie Fault system (Italian eastern Alps). *Tectonics*, 20(6), 999–1020. <https://doi.org/10.1029/2001tc900021>
- Viola, G., Mancktelow, N. S., Seward, D., Meier, A., & Martin, S. (2003). The Pejo Fault system: An example of multiple tectonic activity in the Italian Eastern Alps. *Bulletin of the Geological Society of America*, 115, 515–532. [https://doi.org/10.1130/0016-7606\(2003\)115<0515:tpfsae>2.0.co;2](https://doi.org/10.1130/0016-7606(2003)115<0515:tpfsae>2.0.co;2)
- von Blanckenburg, F., & Davies, J. H. (1995). Slab breakoff: A model for syncollisional magmatism and tectonics in the Alps. *Tectonics*, 14(1), 120–131. <https://doi.org/10.1029/94tc02051>
- Vosteen, H.-D., Rath, V., Clauser, C., & Lammerer, B. (2003). The thermal regime of the Eastern Alps from inversion analyses along the TRANSALP profile. *Physics and Chemistry of the Earth*, 28(9–11), 393–405. [https://doi.org/10.1016/s1474-7065\(03\)00060-3](https://doi.org/10.1016/s1474-7065(03)00060-3)
- Wagreich, M. (2001). Paleocene–Eocene paleogeography of the northern calcareous Alps (Gosau Group, Austria). Paleogene of the Eastern Alps. In W. E. Pier & M. W. Rasser (Eds.), *Österreichische Akademie der Wissenschaften* (Vol. 14, pp. 57–75). Schriftenreihe der Erdwissenschaftlichen Kommissionen.
- Wagreich, M., & Faupl, P. (1994). Palaeogeography and geodynamic evolution of the Gosau Group of the northern calcareous Alps (late cretaceous, eastern Alps, Austria). *Palaeogeography, Palaeoclimatology, Palaeoecology*, 110(3–4), 235–254. [https://doi.org/10.1016/0031-0182\(94\)90086-8](https://doi.org/10.1016/0031-0182(94)90086-8)
- Wallis, S. R., Platt, J. P., & Knott, S. D. (1993). Recognition of syn-convergence extension in accretionary wedges with examples from the Calabrian Arc and the Eastern Alps. *American Journal of Science*, 293(5), 463–495. <https://doi.org/10.2475/ajs.293.5.463>
- Whipp, D. M., Kellett, D. A., Coutand, I., & Ketcham, R. A. (2022). Short communication: Modeling competing effects of cooling rate, grain size, and radiation damage in low-temperature thermochronometers. *Geochronology*, 4(1), 143–152. <https://doi.org/10.5194/gchron-4-143-2022>
- Wiesinger, M., Neubauer, F., & Handler, R. (2006). Exhumation of the Saualpe eclogite unit, Eastern Alps: Constraints from  $^{40}\text{Ar}/^{39}\text{Ar}$  ages. *Mineralogy and Petrology*, 88(1–2), 149–180. <https://doi.org/10.1007/s00710-006-0154-4>

- Willingshofer, E., Neubauer, F., & Cloetingh, S. (1999). The significance of Gosau-type basins for the Late Cretaceous tectonic history of the Alpine-Carpathian belt. *Physics and Chemistry of the Earth - Part A: Solid Earth and Geodesy*, 24(8), 687–695. [https://doi.org/10.1016/s1464-1895\(99\)00100-3](https://doi.org/10.1016/s1464-1895(99)00100-3)
- Wolff, R., Hetzel, R., Dunkl, I., & Anczkiewicz, A. A. (2021). New constraints on the exhumation history of the western Tauern Window (European Alps) from thermochronology, thermokinematic modeling, and topographic analysis. *International Journal of Earth Sciences*, 110(8), 2955–2977. <https://doi.org/10.1007/s00531-021-02094-w>
- Wolff, R., Hetzel, R., Dunkl, I., Anczkiewicz, A. A., & Pomella, H. (2020). Fast cooling of normal-fault footwalls: Rapid fault slip or thermal relaxation? *Geology*, 48(4), 333–337. <https://doi.org/10.1130/g46940.1>
- Wölfler, A., Dekant, C., Danišík, M., Kurz, W., Dunkl, I., Putiš, M., & Frisch, W. (2008). Late stage differential exhumation of crustal blocks in the central Eastern Alps: Evidence from fission track and (U-Th)/He thermochronology. *Terra Nova*, 20(5), 378–384. <https://doi.org/10.1111/j.1365-3121.2008.00831.x>
- Wölfler, A., Dekant, C., Frisch, W., Danišík, M., & Frank, W. (2015). Cretaceous to Miocene cooling of Austroalpine units to the southeast of the Tauern window (Eastern Alps), constraints by multi-system thermochronometry. *Austrian Journal of Earth Sciences*, 108, 18–35.
- Wölfler, A., Frisch, W., Fritz, H., Danišík, M., & Wölfler, A. (2015). Ductile to brittle fault zone evolution in Austroalpine units to the southeast of the Tauern Window (Eastern Alps). *Swiss Journal of Geosciences*, 108(2–3), 239–251. <https://doi.org/10.1007/s00015-015-0193-0>
- Wölfler, A., Kurz, W., Fritz, H., Glotzbach, C., & Danišík, M. (2016). Late Miocene increasing exhumation rates in the eastern part of the Alps – Implications from low temperature thermochronology. *Terra Nova*, 28(5), 297–305. <https://doi.org/10.1111/ter.12221>
- Wölfler, A., Kurz, W., Fritz, H., & Stüwe, K. (2011). Lateral extrusion in the eastern Alps revisited: Refining the model by thermochronological, sedimentary and seismic data. *Tectonics*, 30(4), TC4006. <https://doi.org/10.1029/2010TC002782>
- Wölfler, A., Stüwe, K., Danišík, M., & Evans, N. J. (2012). Low temperature thermochronology in the Eastern Alps: Implications for structural and topographic evolution. *Tectonophysics*, 541–543, 1–18. <https://doi.org/10.1016/j.tecto.2012.03.016>
- Wölfler, A., Wolff, R., Hampel, A., Hetzel, R., & Dunkl, I. (2023). Low-temperature thermochronological data used in the study on the Gurktal Alps (Austria) [Dataset]. Pangaea. <https://doi.org/10.1594/PANGAEA.954973>
- Zaun, P. E., & Wagner, G. A. (1985). Fission-track stability in zircons under geological conditions. *Nuclear Tracks*, 10(3), 303–307. [https://doi.org/10.1016/0735-245x\(85\)90119-x](https://doi.org/10.1016/0735-245x(85)90119-x)
- Zimmermann, R., Hammerschmidt, K., & Franz, G. (1994). Eocene high pressure metamorphism in the Penninic units of the Tauern window (eastern Alps): Evidence from  $^{40}\text{Ar}$ - $^{39}\text{Ar}$  dating and petrological investigations. *Contributions to Mineralogy and Petrology*, 117(2), 175–186. <https://doi.org/10.1007/bf00286841>

## References From the Supporting Information

- Hames, W., & Bowering, S. (1994). An empirical evaluation of the argon diffusion geometry in muscovite. *Earth and Planetary Science Letters*, 124(1–4), 161–167. [https://doi.org/10.1016/0012-821x\(94\)00079-4](https://doi.org/10.1016/0012-821x(94)00079-4)
- Ketcham, R. A., Carter, A., Donelick, R. A., Barbarand, J., & Hurford, A. J. (2007a). Improved measurement of fission-track annealing in apatite using c-axis projection. *American Mineralogist*, 92(5–6), 789–798. <https://doi.org/10.2138/am.2007.2280>
- Ketcham, R. A., Carter, A., Donelick, R. A., Barbarand, J., & Hurford, A. J. (2007b). Improved modelling of fission-track annealing in apatite. *American Mineralogist*, 92(5–6), 799–810. <https://doi.org/10.2138/am.2007.2281>
- Kirschner, D., Cosca, M., Masson, H., & Hunziker, J. (1996). Staircase  $^{40}\text{Ar}$ / $^{39}\text{Ar}$  spectra of fine-grained white mica; timing and duration of deformation and empirical constraints on argon diffusion. *Geology*, 24(8), 747–750. [https://doi.org/10.1130/0091-7613\(1996\)024<0747:saasof>2.3.co;2](https://doi.org/10.1130/0091-7613(1996)024<0747:saasof>2.3.co;2)
- Kuiper, N. H. (1960). Tests concerning random points on a circle. *Proceedings of the Koninklijke Nederlandse Akademie van Wetenschappen, Series A*, 63, 38–47. [https://doi.org/10.1016/s1385-7258\(60\)50006-0](https://doi.org/10.1016/s1385-7258(60)50006-0)
- Wolf, R. A., Farley, K. A., & Silver, L. T. (1996). Helium diffusion and low temperature thermochronology of apatite. *Geochimica et Cosmochimica Acta*, 60(21), 4231–4240. [https://doi.org/10.1016/s0016-7037\(96\)00192-5](https://doi.org/10.1016/s0016-7037(96)00192-5)